Technische Universität München
Fakultät für Physik

Abschlussarbeit im Masterstudiengang Kern-, Teilchen- und Astrophysik

Proto-Neutron-Star Evolution for Different Equations of State Including Muons and Mixing-Length-Convection

Malte Laurenz Heinlein

Max-Planck-Institut für Astrophysik

This edition is a second printing which differs from the original version (25.02.2022) by some minor corrections and annotations. (11.08.2023)

Contents

Chapter 1

Introduction

1.1 The Birth of a Neutron Star

When a star approaches the end of its life the nuclear fire in its core, which has stabilized the star against its own gravity so far, extinguishes. Initially the core is stabilized by the degeneracy pressure of electrons. But for sufficiently massive stars with a birth mass above approximately ten times the mass of our sun photo-disintegration of iron group nuclei robs the core of some of its thermal pressure support, causing an initially slow contraction. Since this contraction results in an increase in density, electron capture on nuclei and free protons becomes more frequent, additionally reducing the pressure support by degenerate electrons causing a further contraction. A fateful feedback cycle of contraction, rising density, and electron captures is started, causing the core to collapse. At the beginning the neutrinos released in the electron captures can escape the collapsing core, but when the density reaches approximately $10^{12}\,\mathrm{g/cm^3}$ the diffusion time scale of the neutrinos exceeds the timescale of the collapse, hence the neutrinos become trapped in the core, and with them lepton number and entropy of the infalling matter, rendering the rest of the collapse adiabatic. Only when the inner part of the core reaches nuclear density of approximately $2.7 \times 10^{14}\,\mathrm{g/cm^3}$ the strong repulsive interactions between nucleons provide enough pressure support against gravity again to enable a new equilibrium, stopping the collapse of the inner core abruptly. However, due to inertia the inner core overshoots this new equilibrium and then bounces back against the still infalling outer layers, starting a shock wave outwards. This shock initially propagates outward against the still infalling overlying layers, but photo-disintegration of nuclei quickly drains the region inside the shock of its thermal pressure support and thus the shock stops still inside the iron core, all velocities inside the shock become negative and the expanding shock transforms into an accretion shock. Since the density inside the shock by approximately this time has decreased to values where the neutrinos can escape, a luminous flash of electron neutrinos released from electron captures is radiated away as the so called ν_e-burst. Matter from overlying layers still infalling through the shock accretes onto the central core, accumulating in a hot, neutrino radiating layer around the forming proto-neutron star (PNS). Shortly after the shock

has stagnated, neutrinos radiated by the contracting and therefore continuously hotter PNS begin to be reabsorbed on nucleons in the matter behind the shock. If this neutrino-heating mechanism, assisted by hydrodynamic instabilities of the matter between the PNS and the shock, i.e. convective overturn and an accretion instability of the shock, is strong enough, neutrinos can deposit enough energy to restart the expansion of the shock. Eventually accretion abades and the still hot and lepton-rich PNS is left behind to evolve toward the final neutron star by the emission of enormous numbers of neutrinos $(\mathcal{O}(10^{58}))$. These neutrinos carry away the gravitational binding energy of the compact remnant and mediate the conversion of the initially proton-rich matter to the neutron-dominated composition of the final neutron star. Approximating the neutron star as a homogeneous sphere of mass M_{NS} and radius R_{NS}, a Newtonian estimate for the gravitational binding energy yields

$$E_{\mathrm{g}} = \frac{3}{5}\frac{GM_{\mathrm{NS}}^2}{R_{\mathrm{NS}}} \approx 2 \times 10^{53}\,\mathrm{erg}\left(\frac{M_{\mathrm{NS}}}{\mathrm{M}_\odot}\right)^2\left(\frac{R_{\mathrm{NS}}}{10\,\mathrm{km}}\right)^{-1}. \tag{1.1}$$

1.2 Proto-Neutron Star Evolution

The PNS deleptonizes by electron neutrino emission and cools by the emission of all kind of neutrinos. With a diffusion argument the timescale for the cooling of the PNS is estimated as

$$\tau_{\mathrm{E}} = \frac{3R_{\mathrm{NS}}^2}{\pi^2 c\lambda}\frac{E_{\mathrm{th}}^0}{2E_\nu^0} \approx 10\,\mathrm{s} \tag{1.2}$$

(Burrows 1984), and for the deleptonization or neutronization of the PNS one gets

$$\tau_L = \frac{3R_{\mathrm{NS}}^2}{\pi^2 c\lambda}\frac{\mathrm{d}Y_{\mathrm{L}}}{\mathrm{d}Y_{\nu_e}} \approx 3\,\mathrm{s} \tag{1.3}$$

(Burrows 1990). Here λ is the initial mean free path of neutrinos in the PNS, R_{NS} the radius of the neutron star, E_{th}^0 and E_ν^0 the initial thermal energy of the neutron star medium and neutrinos respectively, and the derivative $\mathrm{d}Y_{\mathrm{L}}/\mathrm{d}Y_{\nu_e}$ accounts for the refilling of electron neutrinos from the total lepton content of the PNS. As described by Roberts and Reddy (2016), the evolution of the PNS following shock revival can be divided into three subsequent phases:

After shock revival the PNS consists of an inner core of approximately $0.6\,\mathrm{M}_\odot$ of matter at nuclear density formed during the collapse, surrounded by a mantle of approximately $1\,\mathrm{M}_\odot$ of accreted material. Within around one second neutrinos carry away energy and electron number from the mantle, causing it to shrink from a radius around $100\,\mathrm{km}$ to a value close to the final radius of the cold neutron star around $12\,\mathrm{km}$. During this phase the neutrino emission from the PNS is dominated by neutrinos from the contracting mantle and due to a positive temperature gradient

electron anti-neutrinos and heavy lepton neutrinos even diffuse inward from the hot mantle into the comparatively cold core. Deleptonization also moves inward, but does not yet reach the centre of the PNS.

After the mantle has settled onto the core, the neutrino emission from the PNS is dominated by deleptonization moving inward through the PNS. Electron anti-neutrinos and heavy lepton neutrinos still heat the inner core by inward diffusion, while the deleptonization by electron neutrinos causes additional Joule heating (Burrows and Lattimer 1986). Eventually this turns the temperature gradient negative throughout the whole PNS.

Once the chemical potential of electron neutrinos is close to zero throughout the PNS, the compact star continues to contract slowly due to radiating away thermal energy. As the equilibrium electron fraction of nuclear matter decreases with the falling temperature, the PNS still deleptonizes, however on a much slower rate than before. Eventually the PNS becomes transparent for neutrinos, which defines the transition from the PNS phase to the final neutron star, which will continue to cool by neutrino emission for hundreds of years before photons begin to dominate the long-time cooling.

However not only neutrinos can transport energy and lepton number through the PNS but also hydrodynamic flows of matter. While most of the PNS is hydrostatic, due to the spatial and temporal changes in entropy and lepton number gradients there may be regions unstable to convection. Epstein (1979) argued that the mantle is unstable against convection at early times due to the negative lepton number gradient. During the deleptonization and thermal cooling phases also negative entropy gradients can drive convection in the PNS. Convective mass motions are typically very efficient in transporting energy and lepton number and therefore play a crucial role in the PNS evolution.

One crucial ingredient of relevance for the PNS evolution and the associated neutrino emission is the equation of state (EoS) at the extreme conditions in a PNS for densities from far below to several times the nuclear saturation density, temperatures up to more than $50 - 60 \text{MeV}$, and a wide range of proton-to-neutron ratios. The EoS can be decisive for convective instability in the PNS (Roberts et al. 2012b). Furthermore the neutrino opacities due to neutrino-matter interactions depend on the composition of the PNS matter, the chemical potentials of the individual constituents, and also on nucleon interactions, all of which are determined by the EoS (c.f. Roberts and Reddy 2016 for a discussion of contributions to the neutrino opacities relevant in the PNS evolution). In turn this makes the neutrino emission from PNS cooling an intriguing probe of neutrino and nuclear physics at conditions inaccessible to laboratory experiments on earth. Indeed a signal of two dozen electron anti-neutrinos from a stellar core collapse and subsequent PNS cooling event was first (and until now only) detected in 1987 (Bionta et al. 1987, Hirata et al. 1987, Alexeyev et al. 1988), in spatial and temporal correlation with optical observations

of the associated supernova SN1987A, providing observational confirmation of the theoretical picture of core collapse supernovae and PNS evolution.

1.3 Exploration of Proto-Neutron Star Evolution with Simulations

Numerical simulations have been used to study the evolution of PNS for many years, starting the year before SN1987A with the work of Burrows and Lattimer (1986), who employed a grey diffusion scheme for the neutrino transport coupled to quasi-hydrostatic evolution of spherical Tolman-Oppenheimer-Volkoff solutions, later improved by including Ledoux-convection, i.e. convection driven by gradients of entropy and/or lepton-number, via a mixing-length scheme (Burrows 1987), which approximates convective transport of energy and lepton number by an effective one-dimensional treatment using a diffusive description. Burrows (1987) recognized that convective energy and lepton-number transport increases the neutrino luminosities and thus might aid the neutrino-driven shock revival. Wilson and Mayle (1988), using a flux-limited multi-group neutrino diffusion description, expanded this early work on PNS convection, suggesting that salt-finger-like convective activity, driven by different efficiencies of heat and lepton-number transport by neutrinos, can be beneficial for shock revival. Among this early work one should also mention Suzuki and Sato (1991), who also employed flux-limited multi-energy group diffusion to treat the neutrino transport in PNS cooling models with the goal to compare signal predictions with the SN1987A neutrino measurements.

Over the past 30 years since these early studies, a lot of labour has been invested to extend the scope of explored physics and to improve the accuracy of the modelling. This concerns updated and upgraded, more modern input physics on the one hand and better numerical treatments on the other hand. Three lines of progress can be mentioned in this context:

- Investigations of the influence of different models for the nuclear equation of state of hot neutron-star matter. This also includes possible phase transitions at supranuclear density.

- Improvements of the treatment of neutrino transport and the description of neutrino-matter and neutrino-neutrino interactions.

- The advancement from spherically symmetric, thus one-dimensional, modelling, partly with the use of the mixing-length approximation to describe convection in the hot PNS, to direct hydrodynamical simulations in axial symmetry, thus two dimensions, and most recently in three dimensions.

The goal of such studies are better predictions of the neutrino signal that can be expected in terrestrial detectors from a future supernova in our galaxy or repeated efforts to use the measured neutrino events from SN1987A to constrain the nuclear, neutrino and particle physics that plays a role at the extreme conditions in a new-born neutron star.

Neutrino cooling models of nascent neutron stars suffer from our still incomplete knowledge of the physics at supra-nuclear densities and the corresponding high-temperature EoS at neutron-to-proton ratios that can reach far away from isospin symmetry. Therefore considerable attention has been paid to exploring the influence of a large variety of models for the EoS including theoretical descriptions of phase transitions in the supra-nuclear medium. A first study of this kind was performed by Keil and Janka (1995), who considered the influence of the formation of new hadronic states, such as hyperons and Δ-resonances, on PNS evolution, the associated neutrino signal, and the finite-temperature mass limit for black hole formation. Another study of PNS evolution and the associated neutrino signal was performed by Sumiyoshi et al. (1995), who explored the effect of the symmetry energy of nuclear matter in the EoS using two versions of a relativistic mean-field EoS, of which one has an artificially reduced symmetry energy. A later series of works (Pons et al. 1999, Pons et al. 2001b, Pons et al. 2001a) investigated the effects of the possible appearance of hyperons, kaons, or deconfined quarks on PNS cooling, associated neutrino signals, and the evolution of metastable PNS configurations, which collapse to a black hole during the cooling phase. Roberts et al. (2012b) utilized a mixing-length convection scheme and two different EoS to investigate connections between the density dependence of the nuclear symmetry energy and the convective activity in PNS. Recently Nakazato et al. (2022) investigated the expected neutrino signal from a nearby core-collapse supernova in a present detector (Super-Kamiokande) for four EoS employing an quasi-hydrostatic evolution coupled to a multi-energy-group diffusion scheme for the neutrino radiation.

Reliable predictions of the measurable neutrino signal from supernovae and neutron star formation require a most accurate treatment of the neutrino transport and neutrino interactions, which are subsumed in what is called neutrino opacity. While the early works used diffusion descriptions for the neutrino transport, either energy integrated (e.g. Burrows and Lattimer 1986, Burrows 1987, Keil and Janka 1995) or improved by a multi-energy-groups description (e.g. Wilson and Mayle 1988, Suzuki and Sato 1991), more recent simulations were performed with transport solvers that directly integrate the Boltzmann transport equation (e.g. Mezzacappa and Bruenn 1993, Yamada et al. 1999). Alternatively, Rampp and Janka (2002) developed an iterative scheme to solve the neutrino transport problem, the VERTEX code, which couples the Boltzmann moment equations for energy and momentum of the neutrino radiation with the Boltzmann equation to close this non-linear set of integro partial-differential equations. The VERTEX code has been applied for long-time PNS

evolution simulations by Hüdepohl et al. (2010), Hüdepohl (2013), Bollig (2018), and Mirizzi et al. (2016).

Parallel and connected to these works also the description of the neutrino opacities has been gradually upgraded. Suzuki (1993) demonstrated the importance of nucleon-nucleon bremsstrahlung, since it enhances the muon and tau neutrino fluxes. Hüdepohl et al. (2010) found that nucleon-nucleon correlations altering the kinematics of neutrino-matter interactions can shorten the evolution timescales of PNS. Moreover the hierarchy of the mean energies between different neutrino species is affected by the consequences of non-isoenergetic neutrino-nucleon scattering. The importance of mean-field effects on the energy-momentum relation of nucleons for neutrino-nucleon interactions via beta-processes was demonstrated by Martinez-Pinedo et al. (2012) and Roberts et al. (2012a), who found that these effects reduce neutrino luminosities and increase spectral differences between electron neutrinos and anti-neutrinos.

Another important step was the transition from one dimensional simulations to multi-dimensional modelling. This line of work was started by Keil et al. (1996) with the first two-dimensional simulations by solving the hydrodynamic equations for a direct treatment of convection in non-rotating PNS and later including rotation (Janka et al. 2001), following the evolution for more than one second with a equilibrium diffusion treatment for the neutrino transport. Buras et al. (2006) started to upgrade this work by employing the iterative Boltzmann moment solver VERTEX for neutrino transport in this context. Recently Bollig et al. (2017) upgraded such two-dimensional simulations by including, for the first time, muons in the EoS and the description of neutrino-matter interactions. More recently Nagakura et al. (2021) expanded two-dimensional investigations to a large mass spectrum of PNS and to evolution times up to 4 s, although with less sophisticated treatment of neutrino interactions and relatively coarse numerical resolution. Very recently the first rigorous three-dimensional simulations of PNS formation became possible over a period of nearly 2 s, although with an enormous investment of supercomputing resources (Bollig et al. 2021).

However, in this thesis we retreat again to one-dimensional modelling including a mixing-length description of PNS convection, since the presently available contingents of supercomputing power impede calculations of large model sets by three-dimensional or well-resolved two-dimensional simulations. Moreover, a comparison of long-time two-dimensional simulations with one-dimensional PNS evolution calculations including mixing-length treatment of convection has demonstrated good agreement of the predicted neutrino emissions and thus lends support to the application of the mixing-length approximation (Mirizzi et al. 2016).

The PNS evolution calculations discussed in this thesis were carried out with the PROMETHEUS hydrodynamics code in combination with the VERTEX neutrino transport module. The code includes new upgrades to the neutrino-nucleon interactions

by virial corrections (Horowitz et al. 2017) as well as nucleon mean-field corrections (Martinez-Pinedo et al. 2012) for the beta-processes. It also includes the effects of muons in the EoS and neutrino-lepton interactions implemented by Bollig (2018).

The main goal of this thesis is the systematic study of PNS evolution and the associated neutrino emission for different masses of the PNS with a sample of modern finite-temperature EoS that represent state-of-the-art theoretical descriptions and are compatible with all available experimental and and astrophysical constraints, including recent measurements of gravitational waves from a merger event of two neutron stars (GW170817, Abbott et al. 2017), for different masses of the PNS. The neutrino signals obtained from our set of models are planned to be used for a detailed comparison with the SN1987A neutrino data and as a start of a growing library of self-consistently computed supernova neutrino signals for improved predictions of the diffuse supernova neutrino background in dependence on the uncertain supra-nuclear EoS.

In chapter 2 the fundamental equations for describing the evolution of PNS are briefly presented, including a summary of their numerical implementation. In chapter 3 the basic properties of the employed sample of EoS models is described. In chapter 4 we report on the results of our set of PNS evolution simulations for the different EoS and PNS masses. Finally chapter 5 concludes with a short summary of our main findings and an outlook for future work.

Chapter 2

Hydrodynamic and Radiation Transport

2.1 Hydrodynamic

2.1.1 Euler Equations

To follow the core collapse of a massive star, the formation of the hot proto-neutron star, and its subsequent cooling one has to solve the equations for the hydrodynamic of stellar plasma and the equations for the radiation transport of neutrinos together. For the case of negligible viscosity and non-relativistic velocity the hydrodynamic of the stellar plasma is described by the well-known Euler equations. With the sum over i for the three spatial directions implied they read in Cartesian coordinates $(t, \mathbf{x})$

$$\frac{\partial \rho}{\partial t} + \frac{\partial (\rho v_i)}{\partial x_i} = 0 \tag{2.1}$$

describing mass conservation,

$$\frac{\partial (\rho v_j)}{\partial t} + \frac{\partial (v_i \rho v_j + \delta_{ij} P)}{\partial x_i} = Q_{Mj} - \rho \frac{\partial \Phi}{\partial x_j} \tag{2.2}$$

describing momentum conservation for each spatial direction j, and

$$\frac{\partial (\rho \epsilon)}{\partial t} + \frac{\partial (v_i (\rho \epsilon + P))}{\partial x_i} = Q_E + v_i Q_{Mi} - \rho v_i \frac{\partial \Phi}{\partial x_i} \tag{2.3}$$

describing energy conservation. ρ denotes the mass density, v_i a Cartesian component of the velocity $\mathbf{v}$, P the pressure, and $\epsilon = e + \frac{1}{2} \mathbf{v}^2$ the total energy density containing internal energy e and kinetic energy. Rest mass density does not necessarily have to be conserved due to possible nuclear reactions. Therefore we define the mass density $\rho = m_\mathrm{u} n_B$ as a proxy for the conserved baryon number density n_B multiplied with the atomic mass unit $m_\mathrm{u} = 1.66 \times 10^{-24} \, \mathrm{g}$. Φ denotes an external potential, $\mathbf{Q_M}$ and Q_E sources or sinks of momentum and energy which can not be expressed as a potential. In the case of spherical symmetry they reduce to

$$\frac{\partial \rho}{\partial t} + \frac{1}{r^2} \frac{\partial (r^2 \rho v)}{\partial r} = 0, \tag{2.4}$$

$$\frac{\partial(\rho v)}{\partial t} + \frac{1}{r^2}\frac{\partial\left(r^2\rho v^2\right)}{\partial r} + \frac{\partial P}{\partial r} = Q_M - \rho\frac{\partial\Phi}{\partial r}, \tag{2.5}$$

$$\frac{\partial(\rho\epsilon)}{\partial t} + \frac{1}{r^2}\frac{\partial\left(r^2(\rho\epsilon + P)v\right)}{\partial r} = Q_E + vQ_M - \rho v\frac{\partial\Phi}{\partial r} \tag{2.6}$$

in spherical coordinates (t, r). In our case Q_M and Q_E represent exchange of momentum and energy with the neutrino radiation. The potential Φ accounts for the self-gravity of the collapsing star and is determined by the Poisson equation

$$\nabla^2\Phi = 4\pi G\rho \tag{2.7}$$

where G is the gravitational constant. For the spherical symmetric Newtonian case the solution is given by

$$\Phi(r) = -4\pi \int_0^\infty \mathrm{d}r'\, r'^2 \frac{\rho}{|r - r'|}. \tag{2.8}$$

However this set of equations is not closed and therefore requires the pressure to be given as a function of mass density, internal energy, and composition. This is called the equation of state discussed in more detail in chapter 3. As this work is limited to one dimensional models we limit the following discussion to the spherical symmetric case.

2.1.2 Advection of Mass Fractions

Since nuclear reactions, neutrino reactions on nuclei, and advection can change the composition of the stellar plasma and the different species contribute individually to the thermodynamic variables and cross-sections for neutrino interactions an additional equation

$$\frac{\partial(\rho X_j)}{\partial t} + \frac{1}{r^2}\frac{\partial\left(r^2 v\rho X_j\right)}{\partial r} = Q_{Nj}. \tag{2.9}$$

for each species j must be solved to keep track of the chemical evolution. X_j denotes the mass fraction of species j and Q_{Nj} the corresponding source term. Only if the nuclear reactions happen on a much shorter timescale as the hydrodynamical evolution (e.g. in the case of high density and temperature) nuclear statistical equilibrium is established. Then the composition is given as a function of mass density, temperature T, and charge fraction $Y_q = Y_e + Y_\mu$ (the net number of charged leptons per baryon assuming there is no net tauon population) and only the equations

$$\frac{\partial(\rho Y_e)}{\partial t} + \frac{1}{r^2}\frac{\partial\left(r^2 v\rho Y_e\right)}{\partial r} = Q_{Ne}, \tag{2.10}$$

$$\frac{\partial(\rho Y_\mu)}{\partial t} + \frac{1}{r^2}\frac{\partial\left(r^2 v\rho Y_\mu\right)}{\partial r} = Q_{N\mu} \tag{2.11}$$

for net electron number Y_e (the number of electrons less the number of positrons per baryon) and net muon number Y_μ have to be solved to track the chemical evolution.

2.1.3 Mixing-Length Convection

As one dimensional models can not reproduce the inherently multidimensional convection naturally, we use a mixing-length scheme similar to the one by Wilson and Mayle (1988) to account for the additional energy and lepton number transport in convectively unstable regions of the proto-neutron star. In mixing length-schemes the key assumption is that a fluid element in a convectively unstable region once displaced out of its labile equilibrium travels a characteristic distance - the mixing-length - before it mixes with the surrounding medium. This mixing-length l_{mix} is commonly expressed as multiple of the pressure scale height, hence

$$l_{\mathrm{mix}} = \alpha \cdot P / \frac{\mathrm{d}P}{\mathrm{d}r} \tag{2.12}$$

with α as a free parameter of the scheme. The Ledoux criterion identifying convectively unstable regions is given by

$$C_{\mathrm{L}} = - \left. \frac{\partial P}{\partial \rho} \right|_{s,Y_l}^{-1} \cdot \left(\left. \frac{\partial P}{\partial s} \right|_{\rho,Y_l} \frac{\mathrm{d}s}{\mathrm{d}r} + \left. \frac{\partial P}{\partial Y_l} \right|_{\rho,s} \frac{\mathrm{d}Y_l}{\mathrm{d}r} \right) \tag{2.13}$$

where positive values for the Ledoux criterion C_{L} indicate regions unstable against convection and Y_l denotes the net lepton fraction, i.e. the number of leptons (electrons, muons, neutrinos) minus the number of anti-leptons (positrons, anti-muons, anti-neutrinos) per baryon. The Ledoux criterion can be recast into the form (Hüdepohl 2013)

$$C_{\mathrm{L}} = \frac{\mathrm{d}\rho}{\mathrm{d}r} - \frac{1}{c_s^2} \frac{\mathrm{d}P}{\mathrm{d}r} \tag{2.14}$$

so only derivatives with respect to the spatial coordinate and the speed of sound c_s calculated as

$$c_s^2 = \left. \frac{\mathrm{d}P}{\mathrm{d}\rho} \right|_s = \Gamma \cdot \frac{P}{\rho} \tag{2.15}$$

are needed for evaluating the Ledoux criterion. Γ denotes the adiabatic index defined as

$$\Gamma = \left. \frac{\mathrm{d}\log P}{\mathrm{d}\log \rho} \right|_s , \tag{2.16}$$

which is a quantity provided by the EoS. For positive values of the Ledoux criterion the Brunt - Väisälä frequency

$$\omega_{\mathrm{BV}} = \sqrt{-\frac{g}{\rho} C_{\mathrm{L}}} \tag{2.17}$$

with $g = -\partial\Phi/\partial r$ denoting the gravitational acceleration gives a linearised growth rate for convective fluid elements an hence a measure for the strength of convection. Energy conservation implies that a convectively unstable fluid element will attain a velocity

$$v_{\mathrm{mix}} = \sqrt{2g\frac{l_{\mathrm{mix}}^2 C_{\mathrm{L}}}{\rho}}. \tag{2.18}$$

Hence the additional energy flux and lepton fluxes are

$$F_\epsilon = -\rho v_{\mathrm{mix}} l_{\mathrm{mix}} \left(\frac{\mathrm{d}\epsilon}{\mathrm{d}r} + P\frac{\mathrm{d}(1/\rho)}{\mathrm{d}r} \right), \tag{2.19}$$

$$F_{\mathrm{e},\mu} = -\rho v_{\mathrm{mix}} l_{\mathrm{mix}} \frac{\mathrm{d}Y_{\mathrm{e},\mu}}{\mathrm{d}r}. \tag{2.20}$$

These fluxes enter the divergence term of the energy equation (2.6) and the lepton equations (2.10), (2.11) respectively. If nuclear statistical equilibrium does not apply, an equation analogue to (2.20) applies for every nuclear species. In regions of high density where neutrinos are effectively coupled to the medium, neutrino contributions to pressure, energy density, entropy and lepton fraction have to be included in evaluating the Ledoux criterion and convective fluxes.

2.2 Radiation Transport

The neutrinos on the other hand are trapped in the very dense interior of the proto-neutron star and can only slowly diffuse outward but decouple once they reach less dense regions. Therefore we have to solve neutrino transport for the diffusive trapping regime at high density, the free streaming in the thin outer layers of the star, and the intermediate regions. Approximating neutrinos to have vanishing rest mass the Boltzmann equation describing the transport problem reads

$$\frac{1}{c}\frac{\partial f_\nu}{\partial t} + \mathbf{n}\boldsymbol{\nabla}f_\nu = B_\nu \tag{2.21}$$

where c denotes the speed of light, f_ν the distribution function for the neutrinos of species ν, $\mathbf{n}$ the direction of propagation, and B_ν a source term accounting for absorption, emission and scattering. An equation of this type applies to each of the neutrino species $\nu \in \{\nu_e, \bar{\nu}_e, \nu_\mu, \bar{\nu}_\mu, \nu_\tau, \bar{\nu}_\tau\}$. In the following we omit the neutrino species index ν. It is customary to use the specific intensity

$$\mathcal{I}(t, \mathbf{r}, \epsilon, \mathbf{n}) = \left(\frac{\epsilon}{hc}\right)^3 cf \tag{2.22}$$

so that $\mathcal{I}(t, \mathbf{r}, \epsilon, \mathbf{n})\,\mathrm{d}\epsilon\,\mathbf{r}\mathbf{n}/|\mathbf{r}|\,\mathrm{d}\Omega\,\mathrm{d}A\,\mathrm{d}t$ is the energy transported through the normal surface $\mathrm{d}A$ at $\mathbf{r}$ into the solid angle $\mathrm{d}\Omega$ around the direction $\mathbf{n}$ by neutrinos of

energy $[\epsilon, \epsilon + \mathrm{d}\epsilon]$ in the time $[t, t + \mathrm{d}t]$. With $S(t, \mathbf{r}, \epsilon, \mathbf{n}) = (\epsilon/hc)^3 cB$ the Boltzmann equation reads

$$\frac{1}{c}\frac{\partial \mathcal{I}}{\partial t} + \mathbf{n}\boldsymbol{\nabla}\mathcal{I} = S \tag{2.23}$$

or in spherical symmetry

$$\frac{1}{c}\frac{\partial \mathcal{I}}{\partial t} + \mu\frac{\partial \mathcal{I}}{\partial r} + \frac{1 - \mu^2}{r}\frac{\partial \mathcal{I}}{\partial \mu} = S \tag{2.24}$$

where $\mu = \mathbf{n} \cdot \mathbf{r}/|\mathbf{r}|$ denotes the cosine of the angle between the radial direction and the direction of propagation. As above we limit the following discussion to the spherical symmetric case.

Because the source term depends on the intensity and integrals over the intensity (e.g. due to inelastic scattering) this is a four dimensional integro-differential equation. To tame the dimensionality of this problem it is beneficial to use angular moments, where the nth moment is defined as

$$I^{(n)} = \frac{1}{4\pi}\int\limits_{-1}^{+1} \mathrm{d}\mu\, \mu^n \mathcal{I} \tag{2.25}$$

and hence in contrast to the specific intensity the angular moments do not depend on the propagation angle cosine. For the first four moments the labels $J = I^{(0)}$, $H = I^{(1)}$, $K = I^{(2)}$, and $L = I^{(3)}$ are customary. The corresponding integrals of the Boltzmann equation (2.24) yield the moment equations

$$\frac{1}{c}\frac{\partial J}{\partial t} + \frac{1}{r^2}\frac{\partial\left(r^2 H\right)}{\partial r} = S^{(0)}, \tag{2.26}$$

$$\frac{1}{c}\frac{\partial H}{\partial t} + \frac{1}{r^2}\frac{\partial\left(r^2 K\right)}{\partial r} + \frac{K - J}{r} = S^{(1)} \tag{2.27}$$

with the source terms

$$S^{(0)} = \frac{1}{4\pi}\int\limits_{-1}^{+1} \mathrm{d}\mu\, S, \tag{2.28}$$

$$S^{(1)} = \frac{1}{4\pi}\int\limits_{-1}^{+1} \mathrm{d}\mu\, \mu S. \tag{2.29}$$

These source terms couple the neutrino radiation to the hydrodynamic of the stellar

plasma since

$$Q_E = -4\pi \int\limits_0^\infty \mathrm{d}\epsilon \sum_\nu S_\nu^{(0)}, \tag{2.30}$$

$$Q_M = -\frac{4\pi}{c} \int\limits_0^\infty \mathrm{d}\epsilon \sum_\nu S_\nu^{(1)}, \tag{2.31}$$

$$Q_{Nl} = -4\pi m_{\mathrm{u}} \int\limits_0^\infty \mathrm{d}\epsilon \, \frac{S_{\nu_l}^{(0)} - S_{\bar{\nu}_l}^{(0)}}{\epsilon} \tag{2.32}$$

hold. Note that in the first two of the equations above the sum runs over all six neutrino species, whereas the third equation holds for each lepton flavour $l \in \{e, \mu\}$ individually (assuming that there is no net tauon population).

The source terms account for neutrino - neutrino reactions and neutrino - matter reactions. Table 2.1 lists the reactions that enter the calculation of the source term of the Boltzmann equation. The interaction rates for beta reactions and scattering on nucleons account for modifications due to nucleon phase space blocking and nucleon nucleon interactions (Burrows and Sawyer 1998), weak magnetism (Horowitz 2002), quenching of the axial-vector coupling (Carter and Prakash 2002), and reduction of the effective nucleon mass (Reddy et al. 1999). The interaction potentials and effective masses are supplied by the EoS tables discussed in the following chapter.

In using the Boltzmann equation as (2.24) we have assumed an inertial reference frame. However as pointed out by Rampp (2000) it can be beneficial to measure physical quantities (e.g. intensity, source terms) in a frame comoving with the stellar plasma. Furthermore one may consider general relativistic effects. We include gravitational time dilation and red shift but neglect the distinction between proper radius and coordinate radius. In this case the Boltzmann equation for the spherical symmetric case including terms to $\mathcal{O}(\beta)$ becomes (Rampp 2000, Rampp and Janka 2002)

$$\left(\frac{1}{c}\frac{\partial}{\partial t} + \beta\frac{\partial}{\partial r}\right)\mathcal{I} + \mathrm{e}^\Phi\left(\mu\frac{\partial}{\partial r} + \frac{1-\mu^2}{r}\frac{\partial}{\partial\mu}\right)\mathcal{I}$$
$$+ \frac{\partial}{\partial\mu}\left((1-\mu^2)\left(\mu\left(\frac{\beta}{r} - \frac{\partial\beta}{\partial r}\right) - \frac{\partial\mathrm{e}^\Phi}{\partial r}\right)\mathcal{I}\right)$$
$$- \frac{\partial}{\partial\epsilon}\left(\epsilon\left((1-\mu^2)\frac{\beta}{r} + \mu^2\frac{\partial\beta}{\partial r} + \mu\frac{\partial\mathrm{e}^\Phi}{\partial r}\right)\mathcal{I}\right)$$
$$+ \left((3-\mu^2)\frac{\beta}{r} + (1+\mu^2)\frac{\partial\beta}{\partial r} + 2\mu\frac{\partial\mathrm{e}^\Phi}{\partial r}\right)\mathcal{I} = \mathrm{e}^\Phi S \tag{2.33}$$

Table 2.1: Neutrino reactions considered in calculating the source term for the Boltzmann equation in VERTEX. Here (A, Z) denotes a nucleus with mass number A and charge Z, N a nucleon, ν without subscript a neutrino or anti-neutrino of any flavour, ν_x a neutrino or anti-neutrino of μ or τ flavour, and a prime indicates energy exchange between the reaction partners, i.e. inelastic scattering.

Interactions	References
Beta - Processes	
$\nu_e + n \rightleftharpoons e^- + p$	Bruenn (1985), Mezzacappa and Bruenn (1993), Burrows and Sawyer (1999)
$\bar{\nu}_e + p \rightleftharpoons e^+ + n$	ibid.
$\nu_e + (A, Z) \rightleftharpoons e^- + (A, Z-1)$	Bruenn (1985), Mezzacappa and Bruenn (1993), Langanke et al. (2003)
$\nu_\mu + n \rightleftharpoons \mu^- + p$	Lohs (2015), Burrows and Sawyer (1999), Bollig (2018)
$\bar{\nu}_\mu + p \rightleftharpoons \mu^+ + n$	ibid.
Leptonic Absorption	
$\nu_\mu + e^- \rightleftharpoons \nu_e + \mu^-$	Lohs (2015), Bollig (2018)
$\bar{\nu}_\mu + e^+ \rightleftharpoons \bar{\nu}_e + \mu^+$	ibid.
$\bar{\nu}_e + e^- \rightleftharpoons \bar{\nu}_\mu + \mu^-$	ibid.
$\nu_e + e^+ \rightleftharpoons \nu_\mu + \mu^+$	ibid.
Muon Decay	
$\mu^- \rightleftharpoons e^- + \bar{\nu}_e + \nu_\mu$	ibid.
$\mu^+ \rightleftharpoons e^+ + \nu_e + \bar{\nu}_\mu$	ibid.
Scattering	
$\nu + (A, Z) \rightleftharpoons \nu + (A, Z)$	Horowitz (1997), Bruenn and Mezzacappa (1997)
$\nu + (A, Z) \rightleftharpoons \nu' + (A, Z)'$	Langanke et al. (2008)
$\nu + N \rightleftharpoons \nu' + N'$	Bruenn (1985), Mezzacappa and Bruenn (1993), Burrows and Sawyer (1998)
$\nu + e^\pm \rightleftharpoons \nu' + e^{\pm\prime}$	Mezzacappa and Bruenn (1993), Chernohorsky (1994)
$\nu + \mu^\pm \rightleftharpoons \nu' + \mu^{\pm\prime}$	Lohs (2015), Mezzacappa and Bruenn (1993), Chernohorsky (1994), Bollig (2018)
Buras et al. (2003)	
$\nu_x + \{\nu_e, \bar{\nu}_e\} \rightleftharpoons \nu_x' + \{\nu_e', \bar{\nu}_e'\}$	Buras et al. (2003)
Pair Production	
$\nu + \bar{\nu} \rightleftharpoons e^- + e^+$	Bruenn (1985), Pons et al. (1998)
$\nu_{\mu,\tau} + \bar{\nu}_{\mu,\tau} \rightleftharpoons \nu_e + \bar{\nu}_e$	Buras et al. (2003)
Nucleon - Nucleon Bremsstrahlung	
$\nu + \bar{\nu} + N + N \rightleftharpoons N + N$	Hannestad and Raffelt (1998)

and the moment equations read

$$\left(\frac{1}{c}\frac{\partial}{\partial t} + \beta\frac{\partial}{\partial r}\right)J + \frac{1}{r^2}\frac{\partial}{\partial r}\left(r^2 H \mathrm{e}^\Phi\right)$$

$$- \frac{\partial}{\partial\epsilon}\left(\epsilon\left(\frac{\beta}{r}(J-K) + \frac{\partial\beta}{\partial r}K + \frac{\partial\mathrm{e}^\Phi}{\partial r}H\right)\right)$$

$$+ \frac{\beta}{r}(3J-K) + \frac{\partial\beta}{\partial r}(J+K) + \frac{\partial\mathrm{e}^\Phi}{\partial r}H = \mathrm{e}^\Phi S^{(0)} \tag{2.34}$$

and

$$\left(\frac{1}{c}\frac{\partial}{\partial t} + \beta\frac{\partial}{\partial r}\right)H + \frac{1}{r^2}\frac{\partial}{\partial r}\left(r^2 K \mathrm{e}^\Phi\right) + \mathrm{e}^\Phi\frac{K-J}{r}$$

$$- \frac{\partial}{\partial\epsilon}\left(\epsilon\left(\frac{\beta}{r}(H-L) + \frac{\partial\beta}{\partial r}L + \frac{\partial\mathrm{e}^\Phi}{\partial r}K\right)\right)$$

$$+ 2\left(\frac{\partial\beta}{\partial r} + \frac{\beta}{r}\right)H + \frac{\partial\mathrm{e}^\Phi}{\partial r}J = \mathrm{e}^\Phi S^{(1)} \tag{2.35}$$

where $\beta = v/c$ denotes the fluid velocity in units of the speed of light and e^Φ the lapse function. Here all physical quantities are measured in the frame comoving with the stellar plasma, but the coordinates (r, t) are Eulerian.

While in the system of equations (2.26), (2.27) (or (2.34), (2.35)) the direction dependence is removed and hence the dimensionality reduced, the system is not closed. Of course it is in principle possible to calculate higher order moments and the corresponding moment equations, but every moment equation always depends on the next (or next two) higher moment. A common way to solve this problem is to introduce the Eddington factors f_K, f_L so that the higher moments can be expressed as a function of the zeroth moment:

$$f_K = \frac{K}{J}, \tag{2.36}$$

$$f_L = \frac{L}{J}. \tag{2.37}$$

These factors can, for example, be computed from an approximate solution of the Boltzmann equation. This requires the numerical integration of equation (2.33), solving it iteratively together with equations (2.34), (2.35), which provide the input values of J and H needed to express the interaction integral on the right hand side of equation (2.33). This is called variable Eddington factor technique for solving the Boltzmann transport problem.

For comparison of models among each other and with observations it is often

beneficial to use the luminosity

$$L = 16\pi^2 r^2 \int\limits_0^\infty \mathrm{d}\epsilon\, H. \tag{2.38}$$

Defining the normalized neutrino energy spectrum

$$f(\epsilon) = \frac{\int_{-1}^{+1} \mathrm{d}\mu\, \mathcal{I}}{\int_0^\infty \mathrm{d}\epsilon \int_{-1}^{+1} \mathrm{d}\mu\, \mathcal{I}} \tag{2.39}$$

we can write the energy moments of the neutrino radiation as

$$\langle \epsilon^n \rangle = \int\limits_0^\infty \mathrm{d}\epsilon\, \epsilon^n f(\epsilon). \tag{2.40}$$

2.3 Numerical Implementation

For our simulations we use PROMETHEUS-VERTEX. PROMETHEUS is a time-explicit implementation of the Piecewise Parabolic Method of Colella and Woodward (1984) developed by Fryxell et al. (1989). We include the improvements of Keil (1997) allowing for the radial grid to contract during the collapse phase and Kifonidis et al. (2003) who implemented the consistent multi fluid advection scheme of Plewa and Müller (1999) reducing numerical diffusion of nuclear species.

Motivated by a comparison of the Newtonian PROMETHEUS with fully relativistic hydrodynamic codes Marek et al. (2006) developed and tested several effective gravitational potentials to capture relativistic effects with Newtonian hydrodynamics. We utilize *Case A* from this work, hence instead of using equation (2.8) the gravitational potential is computed according to

$$\Phi(r) = -4\pi G \int\limits_r^\infty \frac{\mathrm{d}r'}{r'^2} \left(\frac{m_{\mathrm{TOV}}}{4\pi} + r'^3 \frac{P + P_\nu}{c^2} \right) \frac{1}{\Gamma^2} \left(1 + \frac{\rho\epsilon + P}{\rho c^2} \right) \tag{2.41}$$

with a modified Tolman-Oppenheimer-Volkoff mass

$$m_{\mathrm{TOV}}(r) = \int\limits_0^r 4\pi r'^2 \, \mathrm{d}r' \, \Gamma \cdot \left(\rho + \frac{\rho\epsilon + E_\nu + vF_\nu/\Gamma}{c^2} \right) \tag{2.42}$$

and the metric function

$$\Gamma = \sqrt{1 + \frac{v^2}{c^2} - \frac{2G}{c^2} \frac{m_{\mathrm{TOV}}}{r}} \tag{2.43}$$

where c denotes the speed of light, v the fluid velocity, and E_ν, F_ν, P_ν energy density, energy flux and radiation pressure of the neutrinos.

We follow the implementation of the mixing-length scheme by Hüdepohl (2013) to account for convection in the proto-neutron star, but generalized in one important aspect: In the current version the mixing-length scheme accounts for neutrino contributions in the high density regime by adding contributions from an ideal Fermi gas of neutrinos to energy, pressure, lepton number, and entropy. The corresponding flux of lepton number is added to the electron fraction flux. Thereby an explicit coupling of the mixing-length scheme in the hydrodynamic part of the code to the neutrino solver is avoided.

For the neutrino radiation transport we use VERTEX by Rampp and Janka (2002), an time-implicit Boltzmann solver employing a variable Eddington factor method along the lines described in section 2.2. We use the improvements by Bollig (2018) to account for non vanishing net muon population and the corresponding neutrino-muon reactions. As pointed out by Keil (1997) the time step for the implicit solution of the neutrino transport is computationally expensive. Contrary the time step for the explicit solution of the hydrodynamic is comparatively computationally cheap but limited by the Courant-Friedrichs-Lewy condition. Therefore it is advantageous to split up a transport time step Δt_T into several smaller hydro time steps Δt_H in a manner that $\Delta t_\mathrm{T} = N_\mathrm{H} \Delta t_\mathrm{H}$ holds for an integer N_H and Δt_T is chosen so that radiation moments and hydrodynamic quantities do not change by more than a few percent. The complete problem is then solved with an operator split tactic.

Following the description in Rampp (2000) we give a rough outline of the update procedure starting from a state $\left(\rho^n, v^n, e^n, Y_e^n, Y_\mu^n \right)$ at time t^n. At first the advection (i.e. equations (2.4)-(2.6), (2.10), (2.11) with the right hand side set to zero) is solved for a time step Δt_H. This provisional result is used to calculate the gravitational potential which is then used to add the gravitational sources to energy and momentum. These two steps are repeated N_H times. The resulting intermediate state $\left(\rho^{n+1}, v^*, e^*, Y_e^*, Y_\mu^* \right)$ contains the updates due to advection and gravity over a time step Δt_T. Together with initial guesses for the radiation moments J, H (e.g. from the previous time step) this state is used to calculate the source term S for the Boltzmann equation (2.33). With the right hand side of the Boltzmann equation given rather than being an integral of the intensity, an approximate solution can be computed. This solution provides the Eddington factors closing the moment equations (2.34), (2.35). The solution of the moment equations yields new values for J, H which are used for an improved guess of the right hand side of the Boltzmann equation. In this way the Boltzmann equation and the moment equations are iterated to convergence. Finally the source terms for energy, momentum and lepton number are mapped back to the hydrodynamic grid and used to apply the neutrino effects to the intermediate state giving the fully updated state $\left(\rho^{n+1}, v^{n+1}, e^{n+1}, Y_e^{n+1}, Y_\mu^{n+1} \right)$ at time $t^{n+1} = t^n + \Delta t_\mathrm{T}$.

This implementation has been tested and compared against other codes used to simulate core collapse supernovae (Liebendörfer et al. 2005, Müller et al. 2010, O'Connor et al. 2018).

Chapter 3

Equation of State

As already mentioned before, the system of the Euler equations (2.4)-(2.6) is not closed and solutions therefore need an additional equation providing the gas pressure as a function of the thermodynamic state (i.e. mass density, energy density, and composition or charge fraction). Furthermore the mixing-length convection scheme also requires the pressure and entropy as functions of the thermodynamic state. For the solution of the neutrino radiation transport additionally the chemical potentials of nucleons, electrons, and muons, as well as the effective masses and interaction potentials of nucleons at high density are needed. Therefore we need a so-called equation of state (EoS), describing the thermodynamic conditions of the PNS medium and providing the necessary quantities.

3.1 Equation of State below Nuclear Density

If the mass density is sufficiently smaller than the nuclear density, the stellar plasma can be described as a mix of ideal Boltzmann gases of nuclei and nucleons, Fermi gases of electrons, muons and their respective anti-particles, and a photon gas, taking into account Coulomb lattice corrections. For this regime we employ pre-calculated tables for the contributions of electrons, positrons, and photons by Janka (1995) and for the contributions of muons by Bollig (2018), combined with routines for the Boltzmann gas of nuclei and nucleons, whose composition is either determined by nuclear statistical equilibrium or a simplified treatment of nuclear burning. Since the tables use mass density, charge fraction, and temperature instead of internal energy density as primary variables defining a thermodynamic state, an inversion of the energy temperature relation of the EoS along constant mass density and charge fraction is necessary. The separate contributions are then evaluated for the thermodynamic state defined by mass density, charge fraction, and temperature and added up. A detailed description of this procedure is given by Bollig (2018).

3.2 Equation of State at and above Nuclear Density

However as the mass density and with it the baryon number density approaches nuclear values interactions between the constituents become relevant and physical models more complex than a mix of ideal gases are needed. Therefore we have to use tabulated results from nuclear physics calculations for the baryonic contributions in the high density regime together with the tabulated contributions for electrons, muons, and photons. The determination of the temperature corresponding to a given internal energy density and the evaluation of the equation of state is done analogue to the low-density regime.

Since both theoretical ab initio calculations of strongly interacting many-body systems and laboratory measurements of asymmetric nuclear matter at and above nuclear density are restricted by severe difficulties, the equation of state for the conditions in proto-neutron stars (spanning several orders of magnitude in density up to more than $1 \times 10^{15}\,\mathrm{g/cm^3}$, temperatures from close to zero up to approximately $100\,\mathrm{MeV}$ and charge fractions from one to close to zero) is calculated using effective descriptions. Therefore we employ several different EoS tables for the high density contribution of baryons calculated with different assumptions and descriptions. A common way to characterize a nuclear EoS is to expand the binding energy per baryon E at vanishing temperature in a Taylor series (see for example Oertel et al. 2017)

$$E(x,\delta) = -E_0 + \frac{1}{2}Kx^2 + \delta^2\left(J + Lx + \frac{1}{2}K_s x^2\right) + \mathcal{O}(x^3) \qquad (3.1)$$

where $x = 1/3(n - n_0)/n_0$ is the deviation of the baryon number density n from saturation density n_0 defined by the condition

$$\left.\frac{\mathrm{d}E}{\mathrm{d}n}\right|_{n=n_0,\delta=0} = 0, \qquad (3.2)$$

$\delta = (n_n - n_p)/n$ the isospin-asymmetry (related to the charge fraction by $\delta = 1 - 2Y_q$), E_0 the binding energy of symmetric matter, K the incompressibility, J the symmetry energy, L the slope of the symmetry energy, and K_s the incompressibility of the symmetry energy at saturation density. Table 3.1 gives an overview of the values for these quantities for the EoS used in this work.

Figure 3.1 shows the adiabatic index as function of density and charge fraction and the temperature fixed by the condition of constant entropy for the different EoS in the transition region to saturation density (approximately $2.7 \times 10^{14}\,\mathrm{g/cm^3}$). The gRDF EoS shows a peculiar rise in the adiabatic index below saturation density. This may be an artefact of the treatment of the phase transition.

In the following paragraphs we give a short description of the EoS used in this work following the review by Oertel et al. (2017) and the specific works cited in the
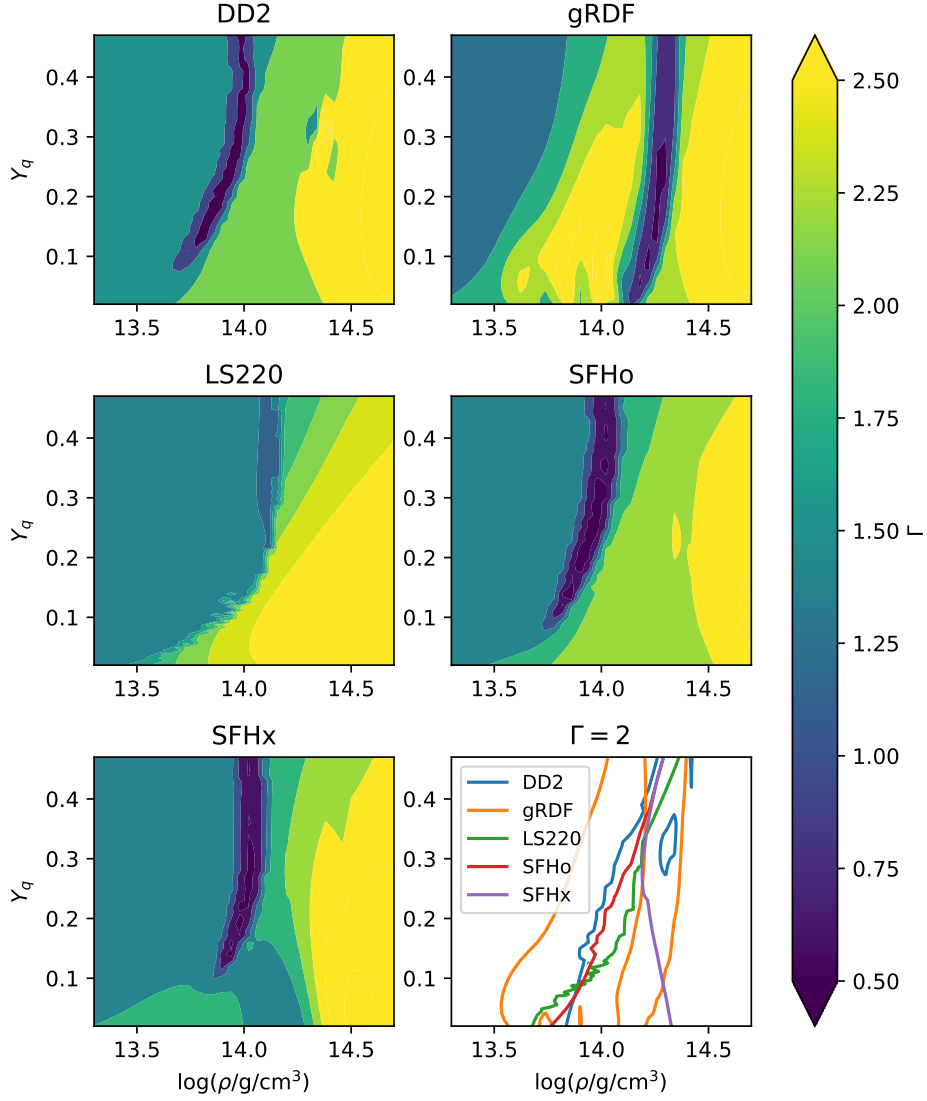
Figure 3.1: Plots of the adiabatic index as function of density and charge fraction at constant entropy of $1.5\,k_B$ per baryon for the different EoS. The lower right panel shows $\Gamma = 2$ isarithms for the different EoS.

Table 3.1: Nuclear properties at saturation density as defined by equation (3.1), radius of a cold 1.4 solar mass neutron star, and maximum gravitational mass for different EoS. Data for DD2, LS220, SFHo, SFHx from Fischer et al. (2014) and *CompOSE*, for gRDF from Typel (2018) and *CompOSE* (`https://compose.obs pm.fr`) entry for GRDF2_DD2. Note that the GRDF2_DD2 differs from the gRDF used in this work, but as both use the same parametrization for nuclear interactions the differences should be small.

EoS	n_0	E_0	K	J	L	K_s	$R_{1.4}$	$M_{\max}$
DD2	0.1491	16.02	243	31.67	55.04	-93.2	13.22	2.42
gRDF	0.149	16.02	243	31.67	55.04	-93.2	13.19	2.42
LS220	0.1550	16.00	220	28.61	73.82	-24.0	12.67	2.05
SFHo	0.1583	16.19	245	31.57	47.10	-205	11.89	2.06
SFHx	0.1602	16.16	238	28.67	23.18	-40.0	11.99	2.13
	$1/\mathrm{fm}^3$	MeV	MeV	MeV	MeV	MeV	km	$M_\odot$

paragraphs. In all cases matter is assumed to be electrically neutral, in thermal, chemical, and mechanical equilibrium, but not necessarily in weak beta equilibrium.

LS220 The EoS from Lattimer and Swesty (1991) uses the Single Nucleus Approximation to describe non-uniform nuclear matter, i.e. below the transition to homogeneous nuclear matter the chemical composition is represented by neutrons, protons, alpha particles, electrons and positrons, photons, and a single species of heavy nuclei with a mean nuclear mass A and charge Z representing the true diversity of heavy nuclei. The latter is known as the single nucleus approximation. At densities below nuclear values the heavy nuclei are treated as a body centred cubic ion lattice embedded in a less dense medium of the other constituents mentioned above with interactions between nucleons, alpha particles and heavy ions treated by an excluded volume formalism. The photon, electron, and positron contributions are treated independently from the baryonic part as non-interacting ultra-relativistic Bose and Fermi gases, respectively. Alpha particles are treated as an ideal Boltzmann gas of hard shells of fixed volume contributing to the excluded volume. The heavy nuclei are described by a compressible liquid drop model with Coulomb term and surface term depending on the filling factor, i.e. the fraction of volume occupied by nuclei, to describe the formation of non-spherical nuclei and bubble phases ("nuclear pasta"). Nucleons are treated as non-relativistic fermions. The nucleon interactions are included as a momentum independent potential model: A density and charge fraction dependent term with free parameters adds to the bulk energy of nucleons. The free parameters are determined by the choice of saturation density, binding energy, incompressibility, and symmetry energy. This approach reproduces

the thermodynamic properties of bulk nuclear matter calculated with Skyrme-type interactions. The same approach is used for the bulk contributions of nucleons in nuclei. A Maxwell construction describes the transition to homogeneous nuclear matter.

DD2 The DD2 EoS from Typel et al. (2010) is based on the work of Hempel and Schaffner-Bielich (2010) which describes non-uniform matter as a mixture of neutrons, protons, light clusters (i.e. deuterons, tritons, 3-helions, and alpha particles), photons, electrons and positrons, and heavy nuclei in nuclear statistical equilibrium. Electrons and positrons are treated as a uniformly distributed non-interacting Fermi gas, photons as ultra-relativistic Bose gas. In contrast to the single nucleus approximation in combination with a liquid drop model used for the LS220, several thousand species of nuclei with tabulated masses are considered. The heavy nuclei are treated as a classical Boltzmann gas. Nuclei and unbound nucleons contribute to the excluded volume like hard spheres with volume $1/n_0$ per baryon, where nucleons and nuclei reduce the volume available to nuclei but only nuclei are considered for the volume excluded for nucleons, as the nucleon-nucleon interactions are treated with a relativistic mean field (RMF) model. Coulomb contributions are calculated assuming spherical Wigner - Seitz cells for every nucleus. Excited states of nuclei at finite temperature are accounted for by an internal partition function for the nuclei. Unbound nucleons are computed as relativistic Fermi gas within a relativistic mean field approach, where nuclear interactions are represented by coupling to a meson field with the nucleon and meson masses as well as the coupling strengths as free parameters. Here the coupling strengths are not constants but functions of the baryon density. These parameters are set by a fit to measurable properties of finite nuclei. A Maxwell construction describes the transition to homogeneous nuclear matter.

SFHo, SFHx The EoS from Steiner et al. (2013) is based on the work of Hempel and Schaffner-Bielich (2010) as well, therefore many aspects of the model are the same as for the DD2 described above. However the key distinction of these EoS is that the free parameters of the RMF model used for the unbound nucleons are determined not only by a fit to laboratory measurements of nuclear properties but also observed neutron star masses and radii. The SFHo fits the mass-radius relation of Steiner et al. (2010), whereas the SFHx attempts to minimize the radius of low mass neutron stars.

gRDF The EoS gRDF in our work is a rather recent offspring of the GRDF2(DD2) from Typel (2018) with a detailed description of some model aspects in Pais and Typel (2017). In contrast to the GRDF2(DD2) (which is also used for table 3.1 and

figure 3.2) the gRDF EoS used in this work was calculated without muons and uses a Maxwell construction for the phase transition to homogeneous nuclear matter. The general relativistic density functional (gRDF) used for this EoS is an extension of the density dependent RMF model used for example for the EoS DD2, SFHo, and SFHx. The model consist of neutrons, protons, two-nucleon correlations as quasi-particles, light clusters, photons, electrons and positrons, and heavy nuclei. As usual electrons, positrons, and photons are treated as non-interacting Fermi and Bose gases. The heavy nuclei are treated as classical Boltzmann gases. Unbound nucleons, the quasi-particle two-nucleon states, and light clusters are treated as relativistic Fermi or Boson gases. Different to the RMF approach all nucleons (including nucleons bound in nuclei) couple to the meson field, however the coupling is scaled according to the nuclei surface for the heavy nuclei. Furthermore all particles are assumed to be point-like, hence there is no excluded volume mechanism. Instead a density and temperature dependent shift of the effective masses is applied facilitating dissolution of nuclei at saturation density. For the nucleon-meson coupling the same parameter set as for the DD2 is used. Coulomb effects are calculated in Wigner - Seitz approximation.

3.3 Slope of Symmetry Energy and Ledoux Convection

Roberts et al. (2012b) pointed out that in particular the slope of the symmetry energy is an interesting parameter for PNS models including convection. Recalling the Ledoux criterion (2.13) and noting that both

$$\left.\frac{\partial P}{\partial \rho}\right|_{s,Y_l}, \left.\frac{\partial P}{\partial s}\right|_{\rho,Y_l}$$

are always positive, for given entropy and electron fraction gradients the sign and magnitude of

$$\left.\frac{\partial P}{\partial Y_l}\right|_{\rho,s} / \left.\frac{\partial P}{\partial s}\right|_{\rho,Y_l}$$

are decisive for convective stability. For negligible neutrino contributions ($P_\nu \ll P, Y_q \approx Y_l$) and negligible temperature the lepton fraction derivative is approximated by (Roberts et al. 2012b)

$$\left.\frac{\partial P}{\partial Y_l}\right|_n \approx \frac{\hbar c}{3}\left(3\pi^2\right)^{1/3} n^{4/3} Y_q^{1/3} - \frac{4n^2}{3n_0}(L + K_s x)\delta \tag{3.3}$$

where the first term on the right hand side is the charge fraction derivative of the pressure of an ultra-relativistic complete-degenerate electron gas and the second term

is derived from equation (3.1)

$$\left.\frac{\partial P_{\mathrm{nuc}}}{\partial Y_q}\right|_n = \left.\frac{\partial}{\partial Y_q}\right|_n \left(n^2 \frac{\partial E}{\partial n}\right) = -\frac{4n^2}{3n_0}(L + K_s x)\delta, \tag{3.4}$$

establishing a connection between the slope of symmetry energy and the Ledoux criterion. Hence for a negative lepton fraction gradient larger values of the density derivative of the symmetry energy act stabilizing against convection. However, equation (3.3) only holds in limited vicinity of the nuclear saturation density, since we only included terms to second order in density in the expansion of the symmetry energy.

3.4 Constraints on the Equation of State

While the physics for the equation of state well below saturation density is mostly understood, the nature of matter at higher densities is still uncertain. However there are some constraints from both laboratory measurements and astronomical observations. Measurements of nuclear masses and charge radii limits possible values for the saturation density and binding energy to $(0.16 \pm 0.01)\,\mathrm{fm}^{-3}$ and $(16 \pm 1)\,\mathrm{MeV}$ respectively (see for example Fiorella and Fantina (2018) and references therein). The nuclear incompressibility can be constrained by measurements of giant monopole resonances of nuclei, but is complicated by dependencies to other nuclear parameters in the evaluation of the measurements (see Oertel et al. 2017 for a short discussion of the problem). Values in the literature range from $(240 \pm 20)\,\mathrm{MeV}$ (Shlomo et al. 2006) to $250\,\mathrm{MeV}$ to $315\,\mathrm{MeV}$ (Stone et al. 2014). The symmetry energy and its slope can be constrained by a variety of measurements and theoretical calculations. The combined analysis of Oertel et al. (2017) yields $(31.7 \pm 3.2)\,\mathrm{MeV}$ for the symmetry energy and $(58.7 \pm 28.1)\,\mathrm{MeV}$ for the slope. While the nuclear parameters of the EoS used in this work (table 3.1) are generally consistent with these constraints, they are in tension with the high values for the incompressibility of Stone et al. (2014). Also the SFHx EoS has a very low slope of symmetry energy compared with these constraints.

Another approach to constrain the EoS for neutron stars is the comparison of model calculations with observed neutron stars. A spherical and cold neutron star may be described by the well known Tolman - Oppenheimer - Volkoff equation and the EoS in the zero temperature limit with the composition determined by beta equilibrium. Under these assumptions it is possible to calculate not only the maximal mass of a neutron star (the famous Tolman - Oppenheimer - Volkoff limit), but also a relation between the neutron star mass and its radius. Figure 3.2 shows these mass-radius relations for the EoS used in this work together with the neutron star mass inferred from observations of the neutron star - white dwarf binary PSR J0348+0432,

with $(2.04 \pm 0.04)\,\mathrm{M_\odot}$ (Antoniadis et al. 2013) one of the most precisely measured neutron star masses above $2\,\mathrm{M_\odot}$, and the mass - radius - relation of Steiner et al. (2010) extracted from observations of x-ray binaries. However the measurement of neutron star radii is complicated, and the inferred values in the literature differ (see for example figure 7 in Oertel et al. (2017) showing radius estimations for the canonical $1.4\,\mathrm{M_\odot}$ neutron star ranging from $8\,\mathrm{km}$ to $16\,\mathrm{km}$). The figure also shows two independent evaluations of x-ray observations of PSR J0740+6620 yielding a neutron star radius from $11.96\,\mathrm{km}$ to $14.26\,\mathrm{km}$ (Miller et al. 2019) or $11.52\,\mathrm{km}$ to $13.85\,\mathrm{km}$ (Riley et al. 2019). We also show limits derived from observations of the binary neutron star merger GW170817 (Bauswein et al. 2017, Abbott et al. 2018). Recently measurements of even heavier neutron stars are reported. Romani et al. (2021) report PSR J1810+1744 with $(2.13 \pm 0.04)\,\mathrm{M_\odot}$, and Cromartie et al. (2020) PSR J0740+6620 with $(2.14 \pm 0.10)\,\mathrm{M_\odot}$.
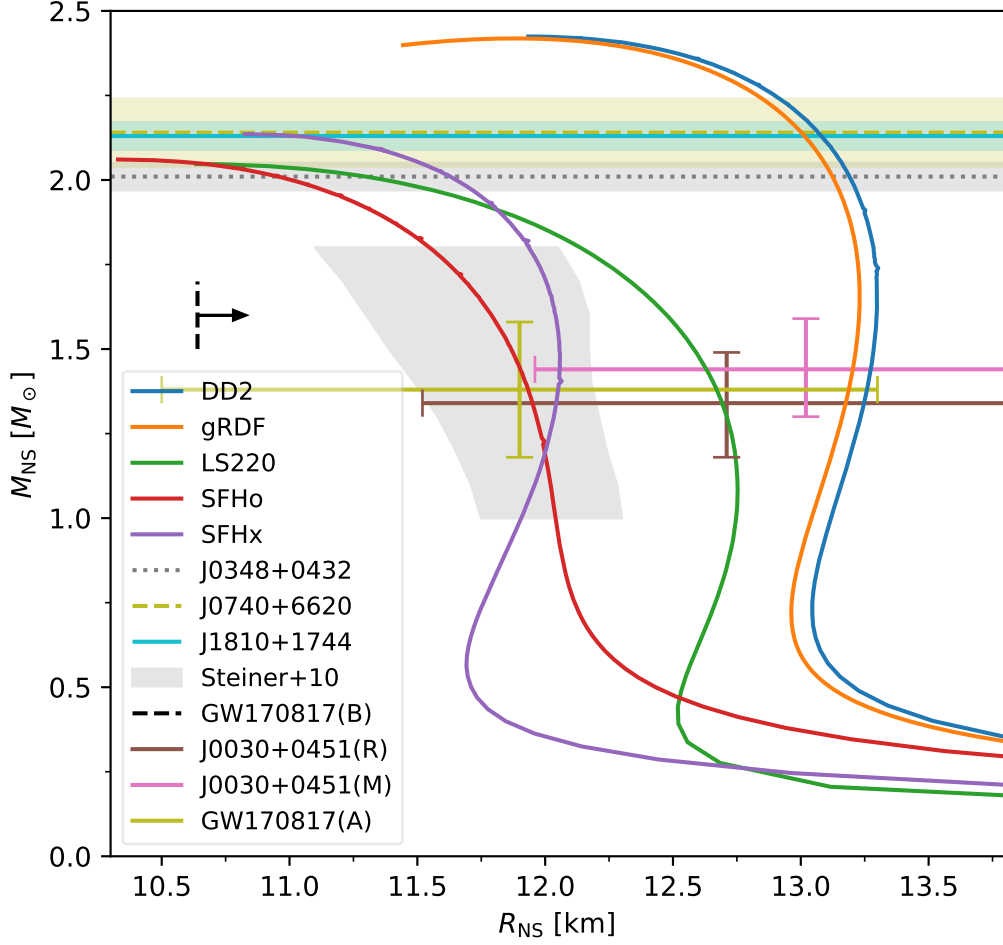
Figure 3.2: Mass-radius relation for cold neutron stars for the different EoS used in this work. Data for the different EoS taken from their respective entry in the *CompOSE* database. Note that the gRDF in this plot is the PT(GRDF2_DD2) which differs from the gRDF used for the simulations. Horizontal colour bands show the one sigma range for neutron star masses of pulsars J0348+0432 (Antoniadis et al. 2013), J0740+6620 (Cromartie et al. 2020), and J1810+1744 (Romani et al. 2021). The shaded region shows the one sigma range of a mass-radius relation derived from X-ray observations (Table 8 in Steiner et al. 2010) used for construction of the SFHo EoS. The black arrow shows the limit for the radius of a $1.6\,M_\odot$ neutron star derived from observations of neutron star merger GW170817 (Bauswein et al. 2017). Furthermore we show the combined limits on mass and radius from the neutron star merger GW170817 (Abbott et al. 2018) and two independent evaluations of x-ray observations of PSR J0030+0451 (Riley et al. 2019, Miller et al. 2019).

Chapter 4

Simulations

4.1 Model Set-up

As progenitors we use four different stellar models advanced to the onset of core collapse, namely the s18.6 and s27.0 models from Woosley et al. (2002), the s20.0 model from Woosley and Heger (2007), and the s18.8 model from Sukhbold et al. (2018). Figure 4.1 shows profiles of the progenitors at the start of the simulation.

Each of these progenitors is advanced through core collapse into the proto-neutron star phase using the five different choices for the EoS listed in chapter 3. Since our one dimensional models do not in general feature successful neutrino driven explosion we initiate them using the recipe of Hüdepohl (2013). Hence after core bounce and accretion we scale down the mass density outside of the shock starting at usually 500 km by a factor of order ten, causing a drop in accretion which allows the shock to expand. As this leads to a nearly complete stop of accretion onto the PNS within some milliseconds, choosing the time for initiating the explosion allows us to determine the mass of the neutron star. For the s18.8 models this is done at the time of bounce, for the s18.6 models 400 ms post bounce, for the s20.0 models 500 ms post bounce, and for the s27.0 models 550 ms post bounce in order to produce models with different neutron star masses. The models are labelled with their progenitor (s18.6, s18.8, s20.0, s27.0) followed by a two letter code indicating the applied high density EoS (DD for DD2, GR for gRDF, LS for LS220, SO for SFHo, SX for SFHx). We define the exact moment of bounce as the time when the entropy per baryon inside the newly formed shock reaches $3.2\,k_B$ for the first time. For the evolution following core bounce we use a time coordinate t_{pb} relative to the moment of bounce t_b as defined above, hence $t_{pb} = t - t_b$. Following the procedure of Bollig 2018 we simulate the collapse phase with electron neutrino transport only, switching to the full six species when the central density reaches $1.4 \times 10^{14}\,\text{g/cm}^3$. Furthermore muons are not included before the core bounce, to avoid complications in disentangling the pressure during the phase transition to nuclear matter. In some exceptional cases the switch to including muons has to be delayed beyond the the moment of core bounce as defined above by some additional 5 ms (s27.0LS) or 10 ms (s18.6GR, s18.8GR, s27.0GR).
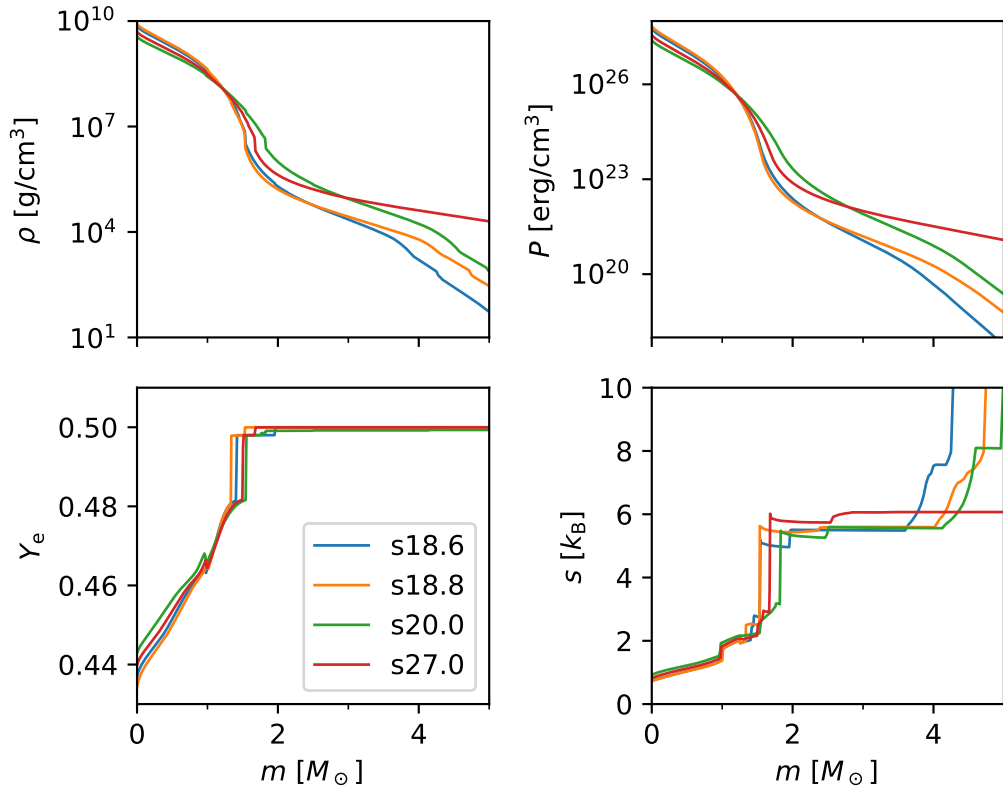
Figure 4.1: Density, pressure, entropy per baryon, and electron fraction as function of the enclosed baryonic mass of the progenitors at the start of our simulations. The entropy profiles show the models with the DD2 EoS. Models with different EoS might differ slightly, since the initialization of the models uses an inversion of the EoS for the pressure given by the progenitors (see Hüdepohl (2013) for a short discussion of the differences between initialization using temperature or pressure as third thermodynamic variable).

In table 4.1 we give an overview over our model set.

4.2 Different Equations of State

In this section we focus on the influence of the applied EoS on the general development of the models. Therefore we limit the discussion to models from one progenitor (s18.6) and explosion time ($t_{pb} = 400\,\text{ms}$), which result in a gravitational neutron star mass of approximately $1.5\,\text{M}_\odot$ at the end of our simulations and discuss snapshots of the models representative for the different evolution stages.

4.2.1 Core Collapse and Bounce

In table 4.2 we give an overview over the duration of the collapse till core bounce, radius of the newly formed shock and the mass enclosed by the shock at the time of core bounce. We see that the collapse duration, shock radius and enclosed mass at bounce mainly depend on the progenitor and not on the EoS. As already pointed out by Hüdepohl (2013) this is expected, since the collapse phase is mainly determined by the progenitor structure and the well constrained physics below saturation density. However the models with the gRDF EoS show noticeable deviations, especially in the shock radius. This might be caused by the early rise of the adiabatic index of the gRDF EoS.

In figure 4.2 we show profiles of density, temperature, electron fraction, and entropy per baryon at the moment of core bounce. We can see that the model with the gRDF EoS indeed bounces at lower density then all other models and also shows an entropy profile clearly differing from the other models. Temperature profiles for the models with DD2, SFHo, and SFHx EoS are rather similar. While the model with the LS220 EoS reaches about the same temperature as the aforementioned at the shock position the inner core does not exhibit a further rise of the temperature but a modest decline. The model with the gruff exhibits a peak in temperature inside the shock alike the DD2, SFHo, and SFHx models in shape, however the temperatures in the core are overall clearly reduced compared to the other models.

Figure 4.3 shows neutrino luminosities and mean energies for the first $40\,\text{ms}$ following core bounce. Here and throughout this thesis we use the energy unit Bethe common in supernova studies, defined as $1\,\text{B} = 10^{51}\,\text{erg}$. Clearly visible is the intense ν_e-burst. The differences between the EoS are small, however a slightly increased mean energy of electron neutrinos for the LS220 around $20\,\text{ms}$ post bounce and slightly decreased luminosities and mean energies for the muon and tau neutrinos and anti-neutrinos for the gRDF around $10\,\text{ms}$ post bounce is observed. An interesting observation is that the hydrodynamic profiles as well as the neutrino emission in this phase is very similar for the models with DD2, SFHo, and SFHx EoS, which are based on the same thermodynamic model and mainly differ in the parametrization

Table 4.1: Overview over our model set. For each model we list model name, the employed nuclear EoS, time post bounce the simulation has reached and the neutron star radius, defined as the $10^{11}\,\text{g/cm}^3$ isodensity radius, gravitational neutron star mass, and baryonic neutron star mass at this time. The column M_{NS} shows the values for the 'gravitational' mass as given in the PROMETHEUS-VERTEX output files. However, this is n o t the true gravitaional mass of the neutron star.

Model	EoS	t_{pb}	R_{NS}	M_{NS}^{G}	M_{NS}^{B}
		s	km	$\text{M}_\odot$	$\text{M}_\odot$
s18.8DD	DD2	10.0	13.6	1.33	1.44
s18.8GR	gRDF	4.23	15.2	1.34	1.44
s18.8LS	LS220	10.0	13.2	1.33	1.44
s18.8SO	SFHo	10.0	12.5	1.32	1.44
s18.8SX	SFHx	10.0	12.5	1.32	1.44
s18.6DD	DD2	10.0	13.9	1.48	1.62
s18.6GR	gRDF	4.55	15.4	1.50	1.62
s18.6LS	LS220	10.0	13.3	1.48	1.62
s18.6SO	SFHo	10.0	12.6	1.47	1.62
s18.6SX	SFHx	10.0	12.7	1.47	1.62
s27.0DD	DD2	10.0	14.0	1.60	1.77
s27.0GR	gRDF	3.15	16.9	1.64	1.77
s27.0LS	LS220	9.29	13.3	1.60	1.77
s27.0SO	SFHo	10.0	12.7	1.59	1.77
s27.0SX	SFHx	10.0	12.7	1.59	1.77
s20.0DD	DD2	10.0	14.0	1.73	1.93
s20.0GR	gRDF	4.04	16.3	1.77	1.93
s20.0LS	LS220	10.0	13.2	1.73	1.93
s20.0SO	SFHo	10.1	12.8	1.72	1.93
s20.0SX	SFHx	10.0	12.9	1.72	1.93

Table 4.2: Time from the start of the simulation till core bounce, the radius of the shock, and the baryonic mass enclosed by the shock at the time of core bounce for the different progenitors and EoS.

EoS	$t_{\rm b}$	$R_{\rm sh}$	$M_{\rm sh}$	$t_{\rm b}$	$R_{\rm sh}$	$M_{\rm sh}$
	s	km	$M_\odot$	s	km	$M_\odot$
		s18.6			s18.8	
DD2	0.256	11.81	0.487	0.237	11.80	0.485
gRDF	0.254	16.13	0.419	0.235	16.20	0.421
LS220	0.242	11.58	0.460	0.224	11.59	0.458
SFHo	0.256	11.06	0.478	0.237	11.10	0.477
SFHx	0.256	10.83	0.476	0.237	10.82	0.473
		s20.0			s27.0	
DD2	0.329	11.94	0.496	0.297	11.85	0.492
gRDF	0.330	15.89	0.410	0.298	15.95	0.414
LS220	0.317	11.53	0.462	0.283	11.53	0.462
SFHo	0.329	11.20	0.486	0.297	11.11	0.482
SFHx	0.329	10.99	0.487	0.297	10.90	0.482

of nucleon interactions, while there are small but in comparison to the other models notable differences for the LS220 and gRDF model. While the LS220 EoS differs both in thermodynamic modelling and parametrization of nucleon interactions from all other EoS, the gRDF employs the same parametrization as the DD2 for nucleon interactions.

4.2.2 Accretion

Figure 4.4 shows density, temperature, electron fraction, and entropy per baryon profiles at 100 ms post bounce. We see the characteristic profile of a nearly unchanged electron fraction in the inner core (up to around $0.4\,M_\odot$) and an already deleptonizing mantle between the inner core and the accretion shock at around $1.5\,M_\odot$. Again we see the most notable variance in the model with the gRDF EoS, the rather peculiar electron fraction profile in the core is likely a relict of the special behaviour of the adiabatic index around bounce. The very flat entropy profile around $1\,M_\odot$ hints at convective mixing being active in this region. The temperature profiles for the models with DD2, LS220, SFHo, and SFHx are similar in shape, but clearly differ in the maximal temperature reached in the mantle at approximately $0.6\,M_\odot$. In the inner core the temperatures for the models with DD2, SFHo, and SFHx are similar, while the the models with LS220 and gRDF reach slightly lower temperatures.

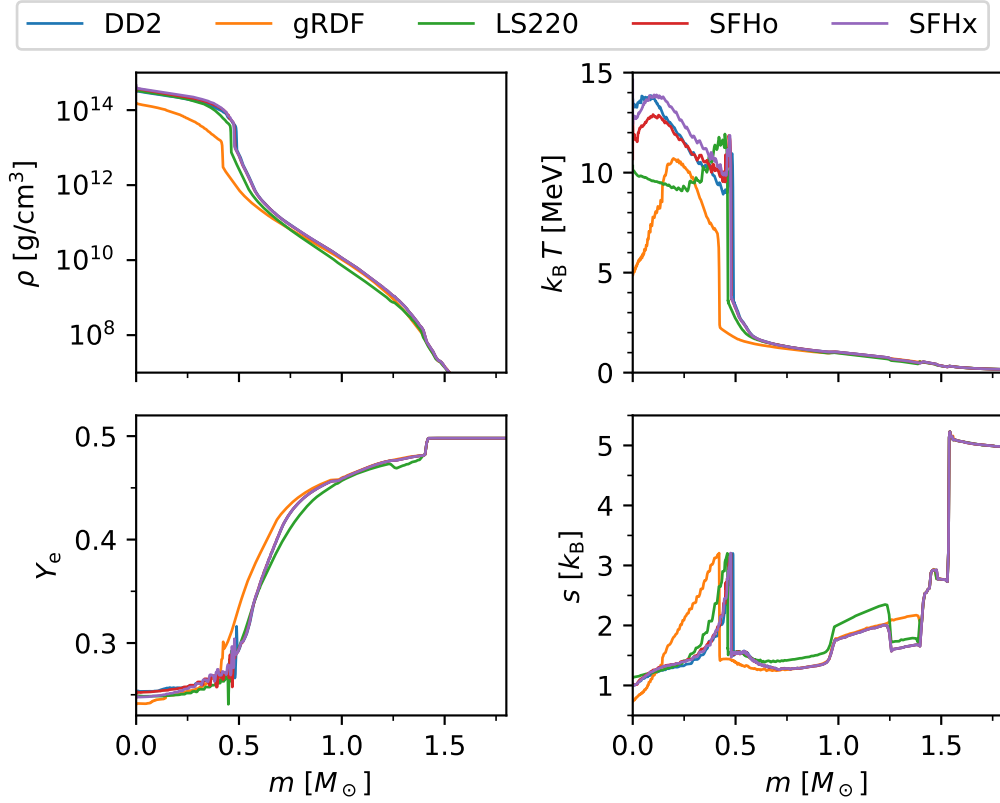Figure 4.5 shows the luminosities and mean energy of neutrino signal for the first

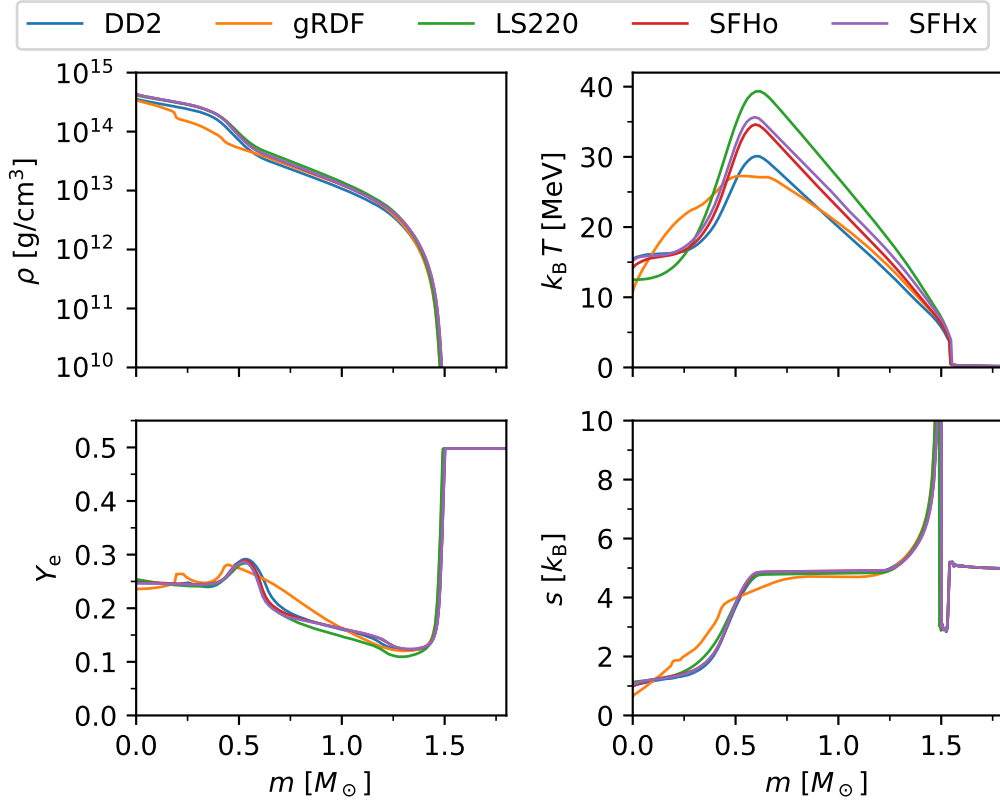Figure 4.2: Density, temperature, electron fraction, and entropy per baryon as function of enclosed baryonic mass at the moment of core bounce ($t_{\mathrm{pb}} = 0$) for s18.6 models with different EoS.

second following core bounce. Clearly visible is the drop of the luminosities shortly after $400\,\mathrm{ms}$ (most pronounced in the electron flavour) due to fading accretion after inserting the density step artificially restarting shock. The mean energies exhibit a clear ordering dependent on the EoS, with the LS220 resulting in the highest mean energies, followed by the SFHo and SFHx, and the DD2 and gRDF resulting in the lowest mean energies.

4.2.3 Mantle Contraction

Figure 4.6 shows density, temperature, electron fraction, and entropy per baryon profiles at $500\,\mathrm{ms}$ post bounce, hence shortly after artificially triggering the shock revival and curbing accretion onto the PNS. By this time the proto neutron star's
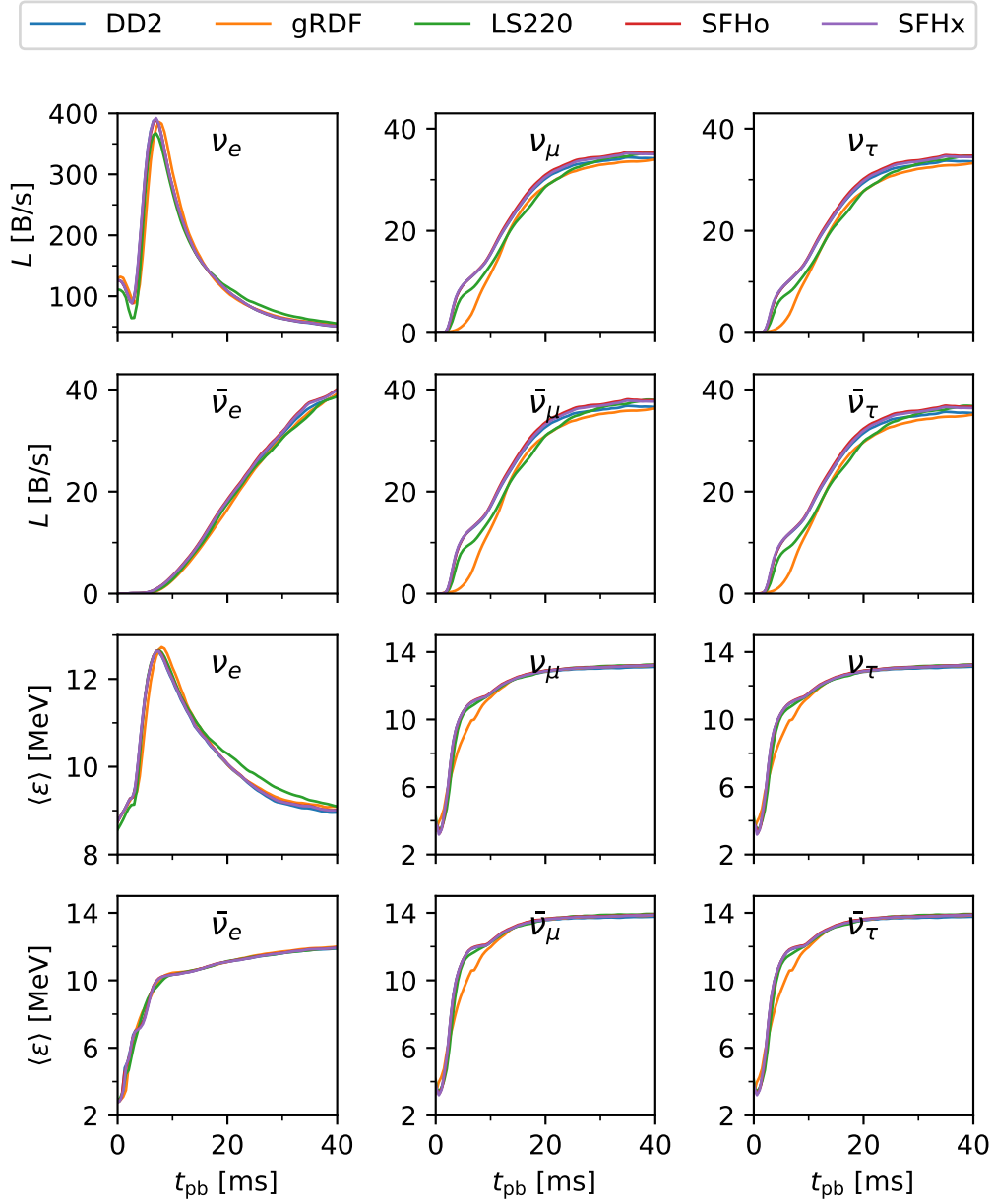
Figure 4.3: Neutrino luminosities and mean energies for the s18.6 models extracted at 500 km as seen by a distant observer. Shown are the first 40 ms post bounce. Note the different scaling of the ordinates for the electron flavours.

Figure 4.4: Density, temperature, electron fraction, and entropy per baryon as function of enclosed baryonic mass at $t_{pb} = 100\,\mathrm{ms}$ for s18.6 models with different EoS.

radius has shrunken from its maximum $\approx 77\,\mathrm{km}$ it reached some tens of milliseconds after bounce to values between $26\,\mathrm{km}$ (LS220), $28\,\mathrm{km}$ (SFHo, SFHx), and $30\,\mathrm{km}$ (DD2, gRDF). As expected higher neutrino luminosities cause quicker contraction. Of course this replicates in the density profiles, with the LS220 model exhibiting the highest densities, followed by the SFHo and SFHx models, and the DD2 and gRDF exhibiting the lowest densities. Compared to the profiles at $100\,\mathrm{ms}$ we can observe an increased maximal temperature in the mantle, with the ordering between the different EoS the same as at $100\,\mathrm{ms}$, i.e. LS220 exhibits the highest temperatures, followed by SFHo and SFHx, followed by DD2 and gRDF. The transition from the flat entropy zone in the mantle to sudden rise at the PNS boundary has sharpened. The peak in electron fraction at the interface of inner core and mantle is nearly levelled.

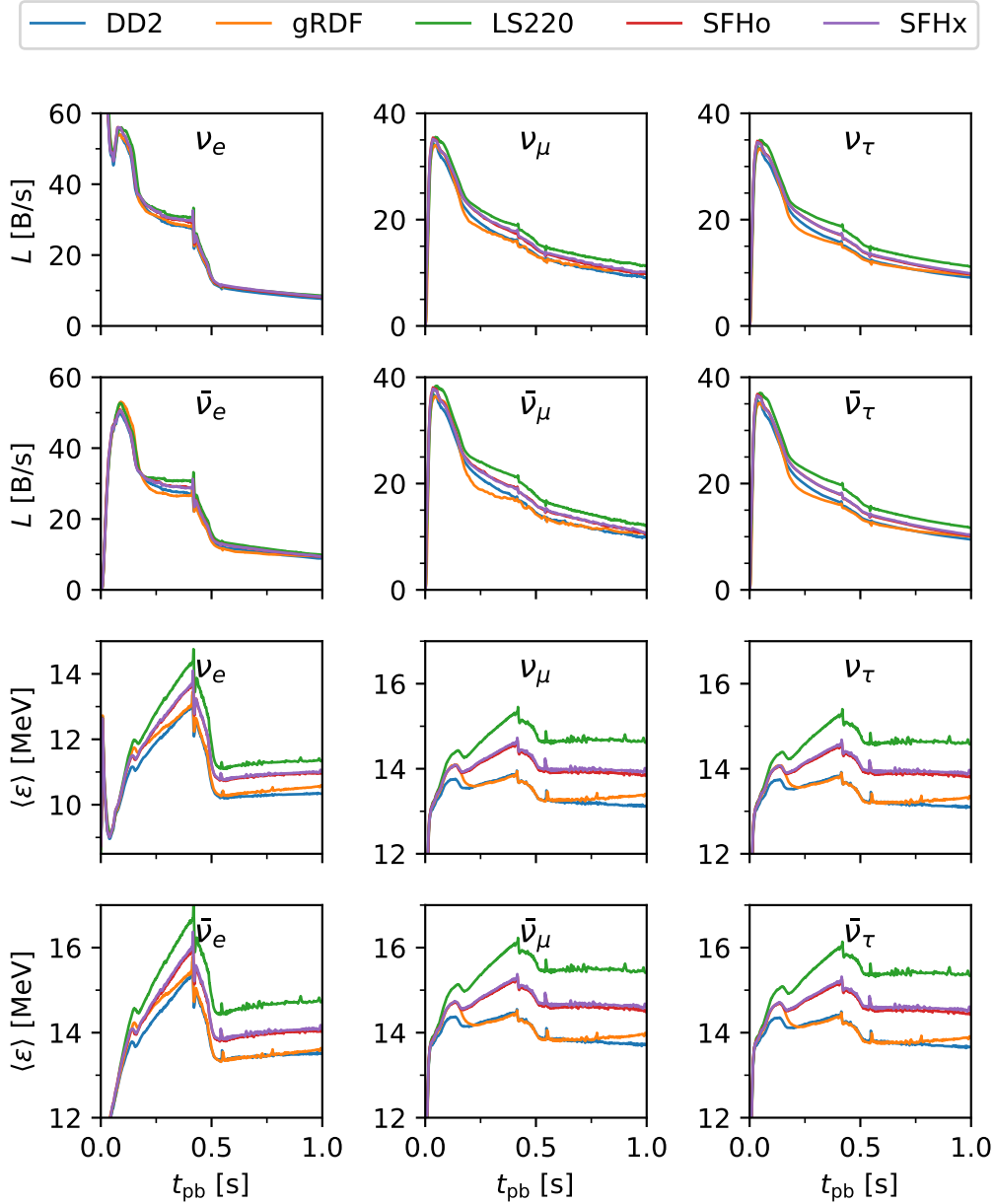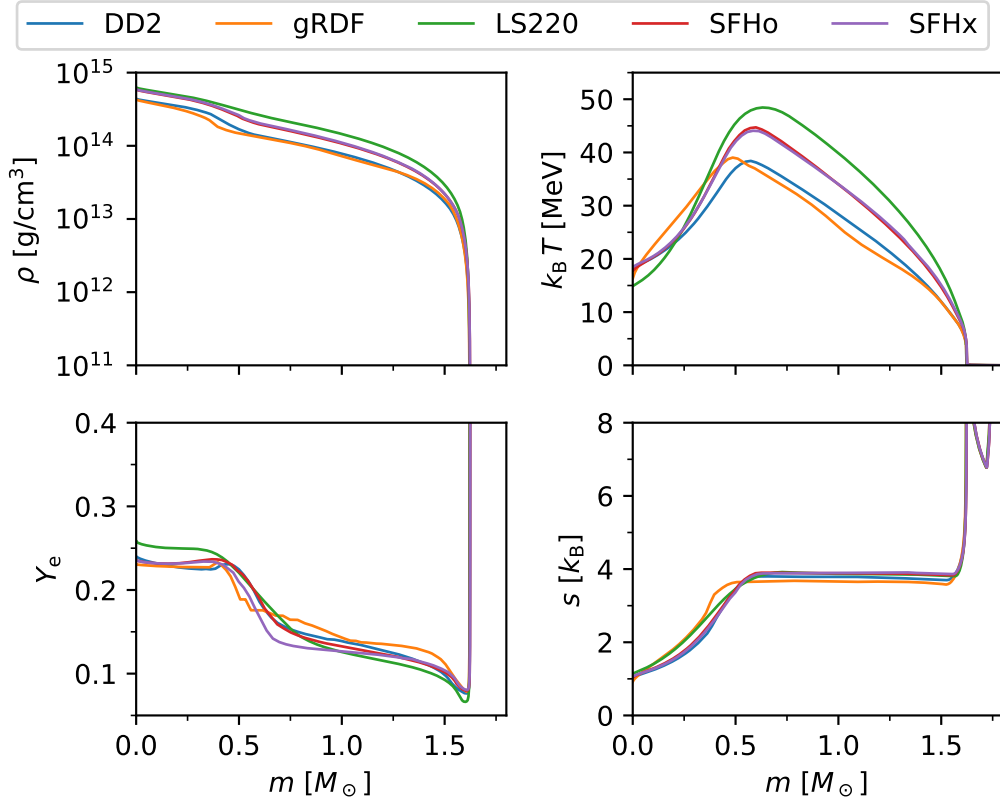Figure 4.7 shows density, temperature, electron fraction, and entropy per baryon

Figure 4.5: Neutrino luminosities and mean energies for the s18.6 models extracted at 500 km as seen by a distant observer. Shown is the first 1 s post bounce. Note the different scaling of the ordinates for the electron flavour. The models with the SFHo and SFHx EoS are nearly concurring, as are the models with gRDF and DD2 EoS after approximately 300 ms until approximately 700 ms. The sharp drop most pronounced in the electronic flavours shortly after 400 ms is caused by artificially restarting shock expansion (see section 4.1).

Figure 4.6: Density, temperature, electron fraction, and entropy per baryon as function of enclosed baryonic mass at $t_{\mathrm{pb}} = 500\,\mathrm{ms}$ for s18.6 models with different EoS.

profiles at $1\,\mathrm{s}$ post bounce. By this time the proto neutron star's radius has shrunken to $20\,\mathrm{km}$ (LS220), $22\,\mathrm{km}$ (SFHo, SFHx), and $24\,\mathrm{km}$ (DD2, gRDF). Compared to our previous snapshot at $500\,\mathrm{ms}$ we observe a reduction in the entropy of the mantle. By now the electron fraction gradient is negative throughout the PNS for all EoS. The ordering of the temperatures in the mantle has changed. The SFHo model now reaches about the same maximal temperature as the LS220 model, the SFHx model follows with small difference, followed by the DD2 and gRDF models.

4.2.4 Deleptonization

Figure 4.8 shows density, temperature, electron fraction, and entropy per baryon profiles at $2\,\mathrm{s}$ post bounce. Both the peak in temperature and the decline of electron
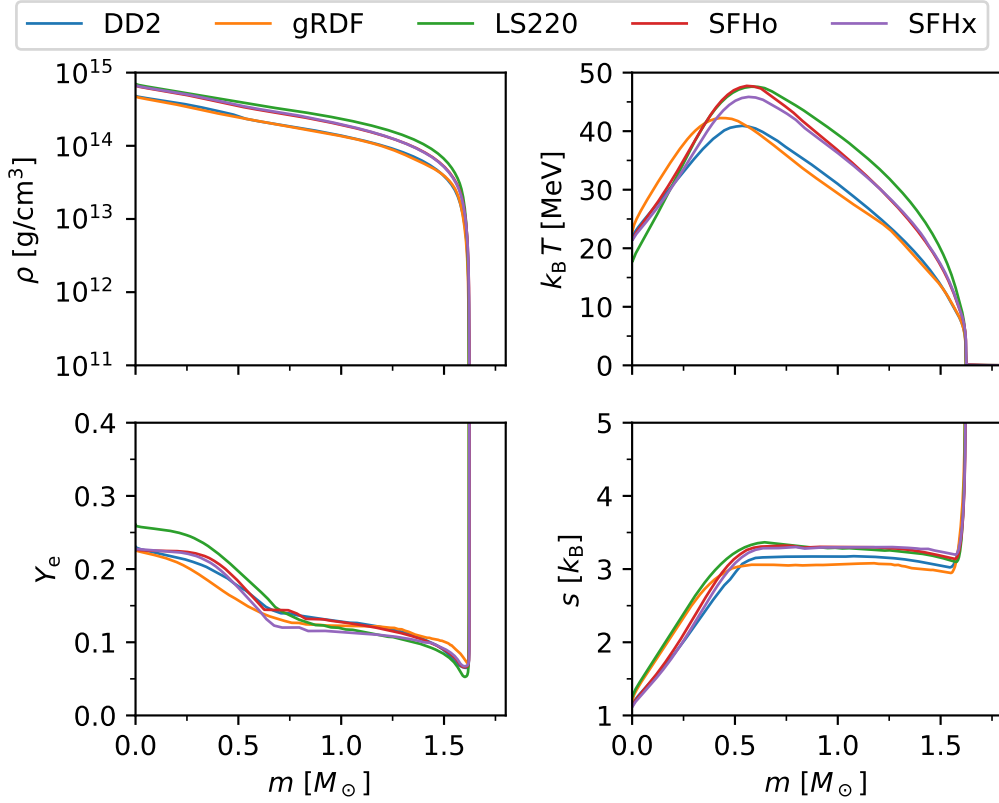
Figure 4.7: Density, temperature, electron fraction, and entropy per baryon as function of enclosed baryonic mass at $t_{\mathrm{pb}} = 1\,\mathrm{s}$ for s18.6 models with different EoS.

number initially placed at the core mantle interface moved inward compared to our last snapshot, the deleptonization of the core starts.

Figure 4.9 shows density, temperature, electron fraction, and entropy per baryon profiles at 4 s post bounce. The deleptonization has reached the centre of the PNS in the case of the models with DD2, gRDF, and SFHo EoS causing a reduction in the central electron fraction which retained its values from core bounce nearly unchanged in the previous snapshots. In the case of the models with SFHx and LS220 the deleptonization is already very close to the centre. The peculiar phase transition behaviour of the gRDF EoS is still visible, but has moved outwards in mass to around $1.5\,\mathrm{M}_\odot$ due to the rising densities in the centre. Compared to the previous snapshots the temperature profiles have changed. The peak has reached the centre, leaving behind a negative temperature gradient throughout the PNS. Also the maximal temperatures started to fall. The model with the LS220 EoS now, except
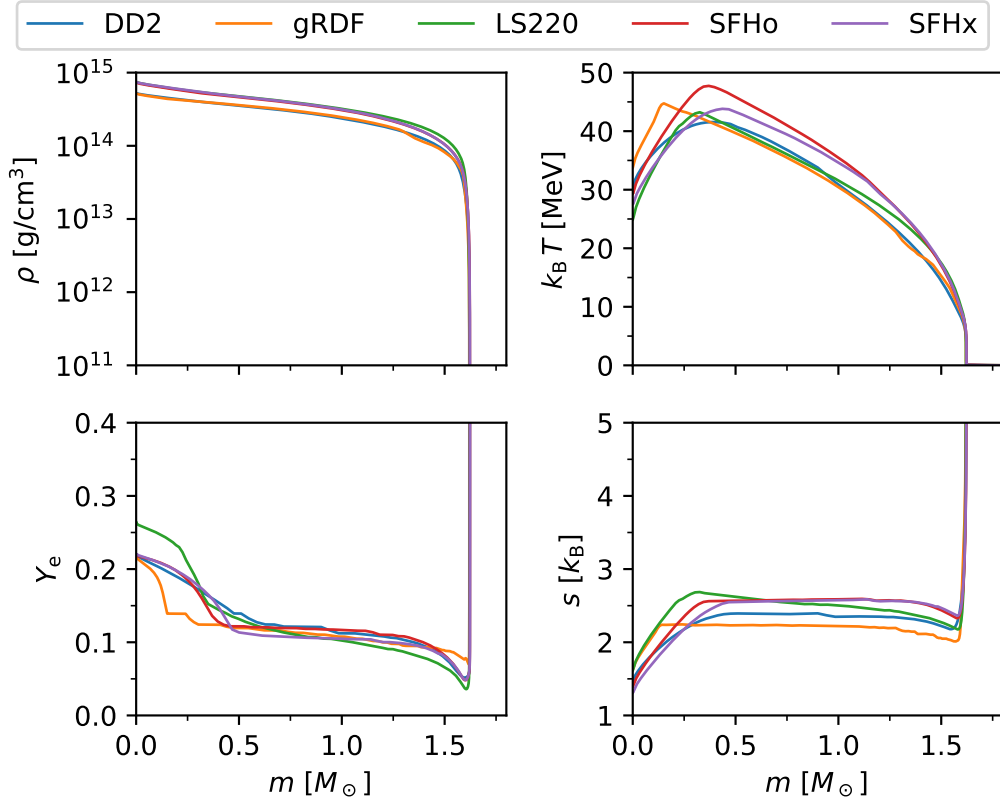
Figure 4.8: Density, temperature, electron fraction, and entropy per baryon as function of enclosed baryonic mass at $t_{\mathrm{pb}} = 2\,\mathrm{s}$ for s18.6 models with different EoS.

for the very centre, exhibits the lowest temperatures, while the other models kept their order relative to each other. While the entropy and electron fraction profiles are now flat from the centre to close beneath the surface of the PNS for the other four models, the model with the LS220 EoS exhibits negative gradients. Due to numerical difficulties the model with the gRDF EoS currently ends shortly after this snapshot.

Figure 4.10 shows density, temperature, electron fraction, and entropy per baryon profiles at 8 s post bounce. The profiles of the models with SFHo and SFHx EoS are very similar again, after differing in temperature in our last three snapshots. The temperatures of all our models has fallen significantly. Similar to the previous snapshots the model with the LS220 exhibits steeper gradients in electron fraction and entropy as the other models.

Figure 4.11 shows the luminosities and mean energy of the neutrino signal for
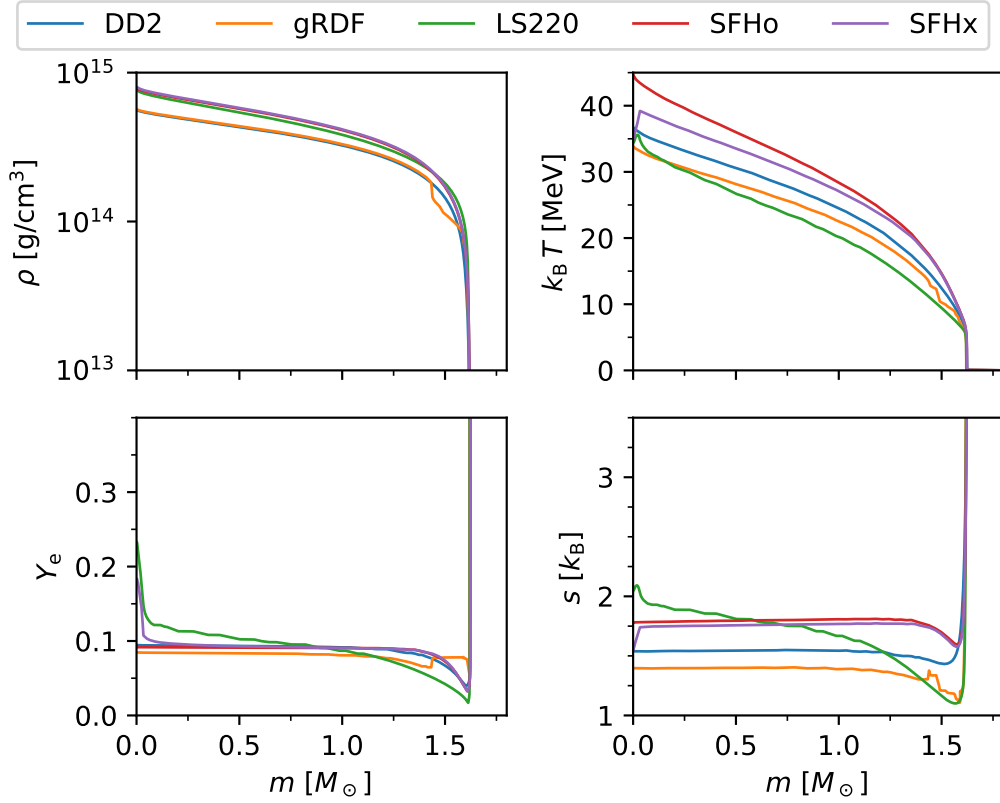
Figure 4.9: Density, temperature, electron fraction, and entropy per baryon as function of enclosed baryonic mass at $t_{\mathrm{pb}} = 4\,\mathrm{s}$ for s18.6 models with different EoS.

$1\,\mathrm{s}$ to $3\,\mathrm{s}$ post bounce. The mean energies still exhibit a clear dependency on the EoS. However, different to the situation during the first second (cf. figure 4.5) the ordering between the different EoS changes. Starting from the configuration at one second with the LS220 resulting in the highest mean energies, followed by the SFHo and SFHx, and the DD2 and gRDF resulting in the lowest mean energies the mean energies and luminosities of the model with the gRDF EoS rise peculiarly for around one second before falling below their initial values again. The mean energies of the model with the LS220 EoS start to drop comparatively quickly around $2\,\mathrm{s}$ post core bounce.

Figure 4.12 shows the luminosities and mean energy of the neutrino signal for $3\,\mathrm{s}$ to $10\,\mathrm{s}$ post bounce. The luminosities and mean energies of the LS220 model continue to drop quickly until around $5\,\mathrm{s}$ post bounce, making them the lowest until the corresponding quantities of the DD2 model, which start to drop around $5\,\mathrm{s}$ post
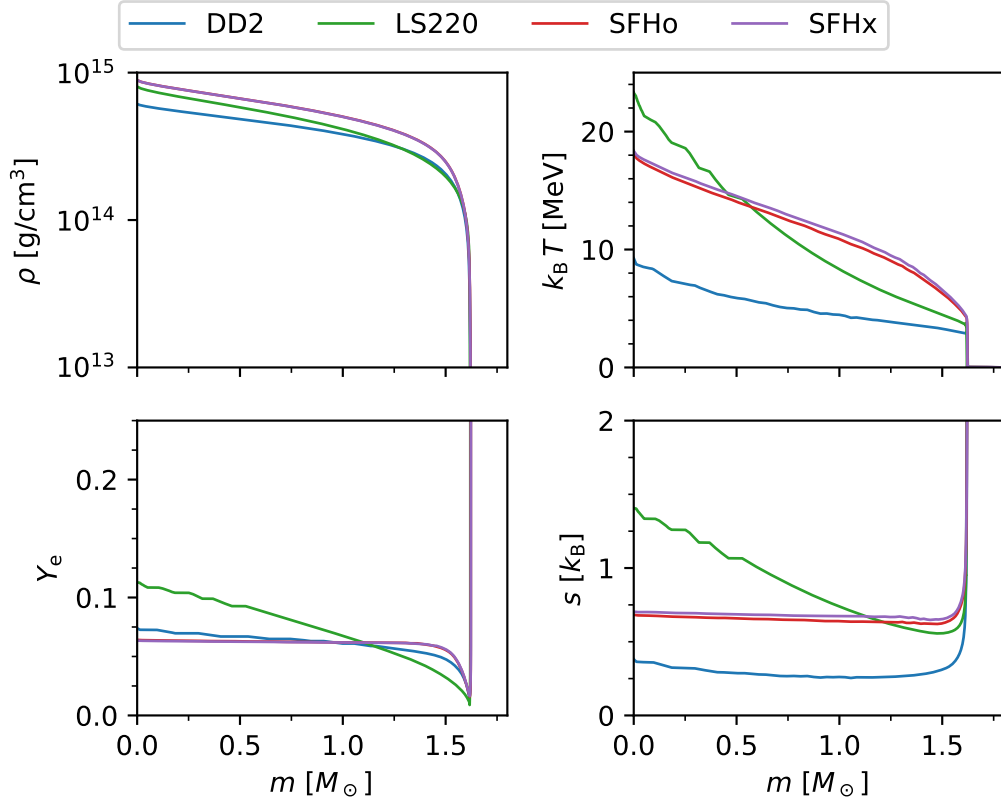
Figure 4.10: Density, temperature, electron fraction, and entropy per baryon as function of enclosed baryonic mass at $t_{\mathrm{pb}} = 8\,\mathrm{s}$ for s18.6 models with different EoS.

core bounce, fall below them again at around $7\,\mathrm{s}$ post bounce. SFHo and SFHx remain very similar till the end of our simulations.
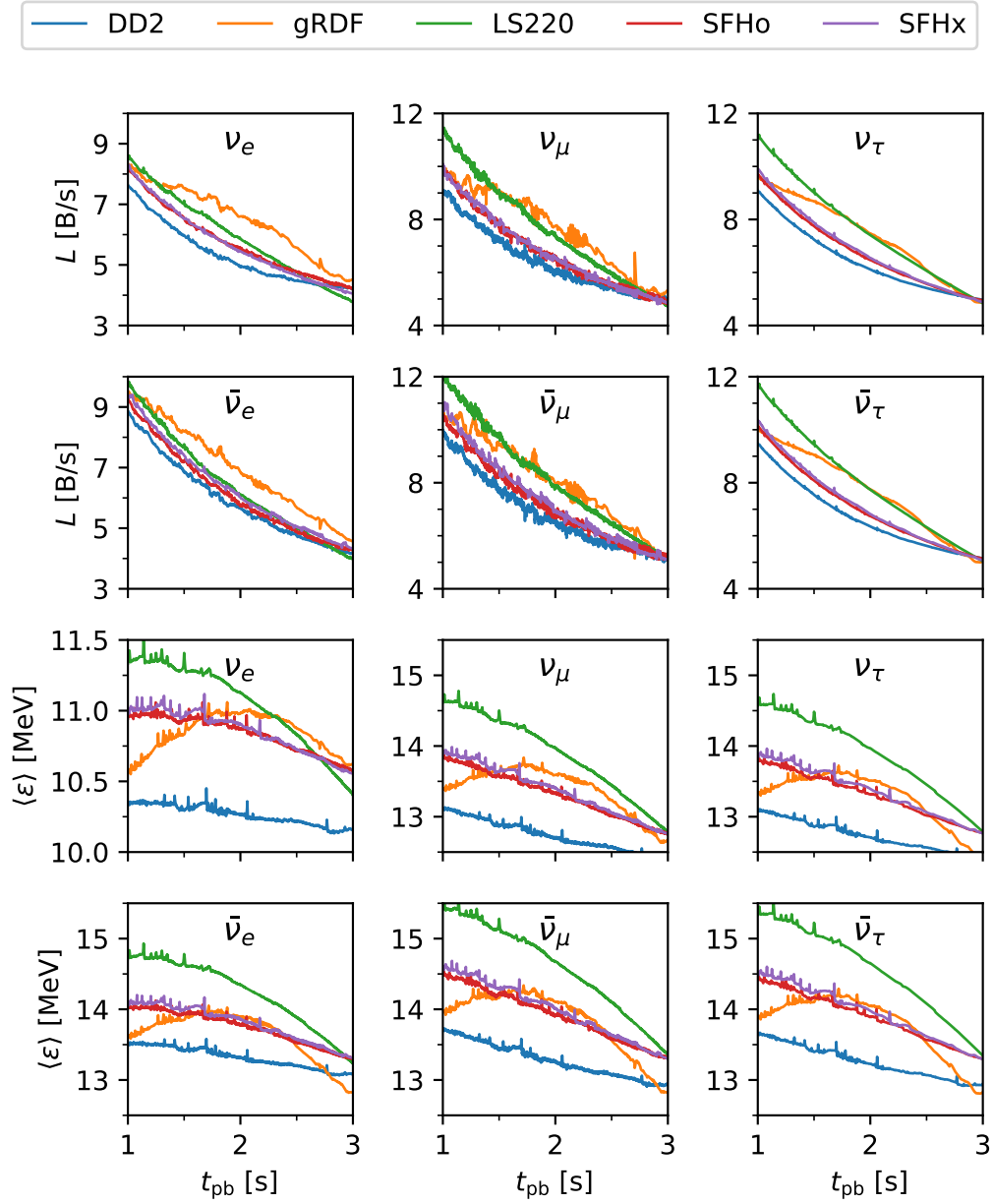
Figure 4.11: Neutrino luminosities and mean energies for the s18.6 models extracted at 500 km as seen by a distant observer. Shown are 1 s to 3 s post bounce evolution of our models. Note the different scaling of the ordinates for the electron flavour.
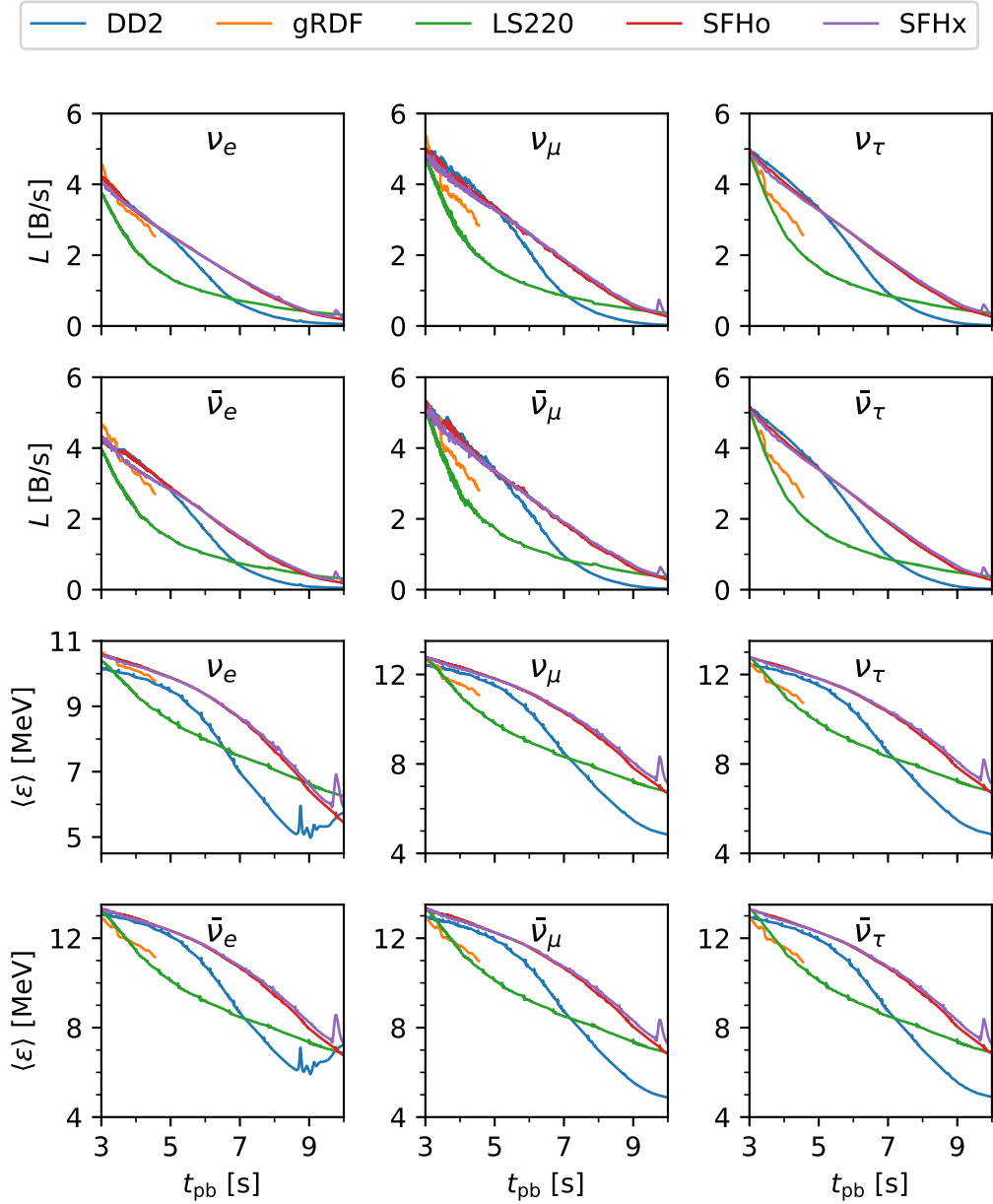
Figure 4.12: Neutrino luminosities and mean energies for the s18.6 models extracted at 500 km as seen by a distant observer. Shown are 3 s to 10 s post bounce evolution of our models. Note the different scaling of the ordinates for the electron flavour. The simulation for s18.6GR currently ends shortly after 4 s post bounce.

4.3 Convection in Models with Different Equations of State

As already mentioned in 3.3 Roberts et al. (2012b) found that the nuclear EoS, in particular the slope of the symmetry energy, can have a decisive influence on the convective activity in PNS. They find that a larger slope of symmetry energy increases the stabilizing effect of negative electron fraction gradients. Unfortunately the Ledoux criterion including the neutrino contributions at high densities is not easily available from our simulation output. However, since convection usually is very efficient in transporting entropy and electron number, regions unstable against convection are quickly driven into marginal stability when applying a mixing-length scheme by flattening of the respective gradients. We therefore take a closer look at the evolution of the entropy and electron fraction and the respective radial gradients in our models.

Figures 4.13 to 4.17 show the temporal evolution of the electron fraction and entropy per baryon and the respective radial gradients in the PNS for the s18.6 models with different EoS.

In all five models we can see a clear separation between the inner core with electron fractions moderately above and entropies moderately below the overlaying mantle. Core and mantle are clearly separated by a thin region of negative electron fraction gradient, initially ($t_{\mathrm{pb}} = 0\,\mathrm{s}$) located slightly above $100\,\mathrm{km}$. While the inner core and the surface just beneath the neutron star radius exhibits positive entropy gradients, a layer of $0.8\,\mathrm{M}_\odot$ to $1\,\mathrm{M}_\odot$ between is essentially flat. We assume this to be the convectively mixed region.

The inner boundary of the convective regions gradually moves inward over a timescale of some seconds until it reaches the centre. However, the exact time until the inner boundary of the convection zone reaches the centre is model dependent. For the case of the s18.6GR model this takes only around $2.5\,\mathrm{s}$, for the s18.6DD around $3\,\mathrm{s}$, for the s18.6SO around $3.4\,\mathrm{s}$, for the s18.6SX around $4.4\,\mathrm{s}$, and for the s18.6 around $4.5\,\mathrm{s}$. As mentioned before, gRDF and DD2 EoS share the parametrization of nucleon interactions and therefore have the same slope of symmetry energy and compressibility of symmetry energy, yet the time until the inner boundary reaches the centre differs slightly. Also the SFHo EoS has a smaller slope of symmetry energy and compressibility of symmetry energy than the DD2 or gRDF EoS, but in the s18.6SO model the inner boundary of the convection zone still takes longer to reach the centre.

Previous studies (Roberts et al. 2012b, Hüdepohl 2013) showed that the outer boundary of the convective zone follows the inner boundary with a delay of some seconds in moving inward. Unfortunately we are not able to track the outer boundary of the convection zone in the same way as the inner boundary, as the electron fraction

profiles and entropy profile in the outer regions stay mostly flat for the rest of the simulation. Therefore we can neither determine the end of convective activity in the PNS nor the size of the convective zone and can not directly compare our results to aforementioned works.
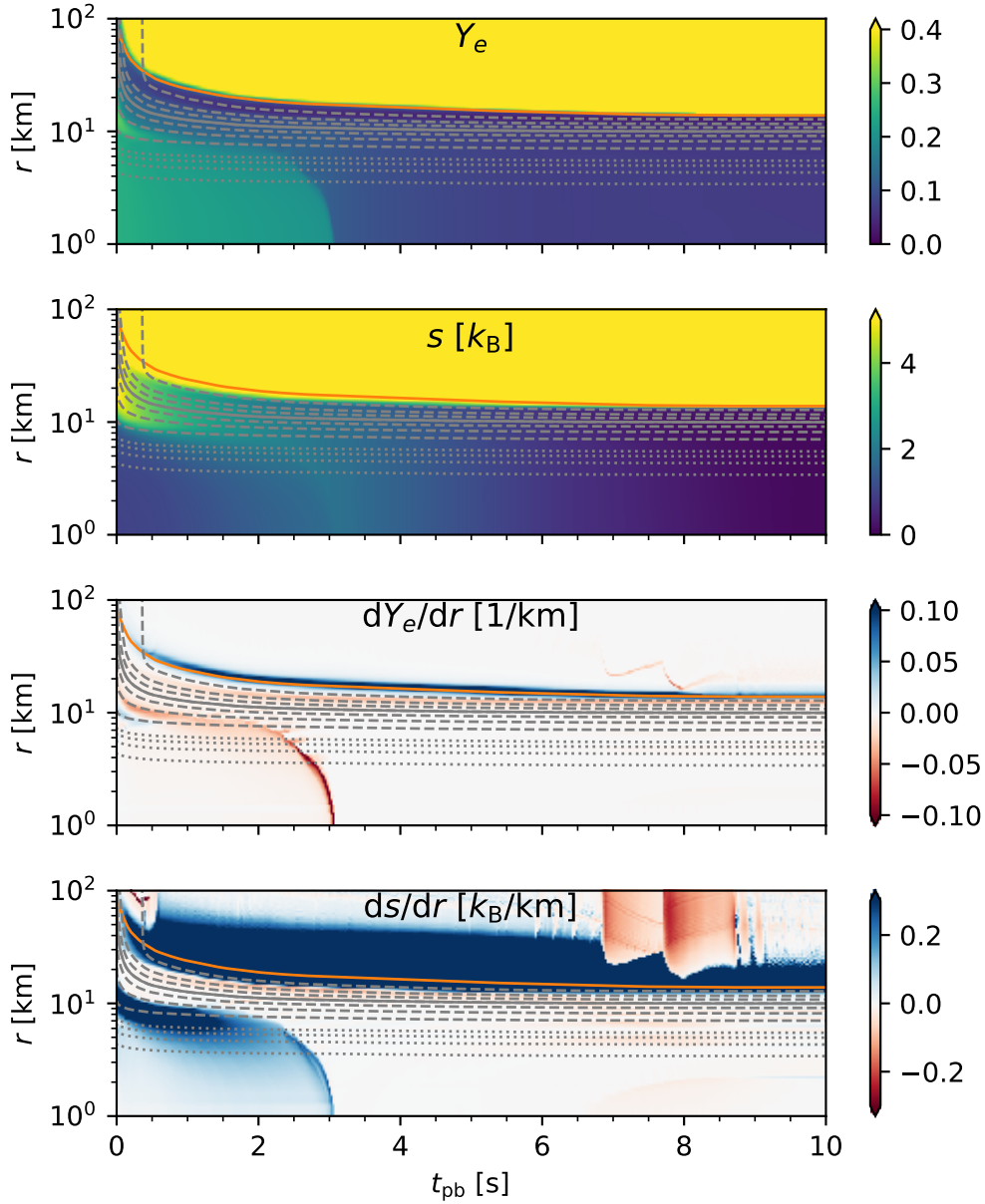
Figure 4.13: Electron fraction and entropy per baryon and radial gradients thereof for model s18.6DD. The orange line indicates the neutron star radius. Grey lines are mass shells of $0.05\,M_\odot$ (dotted) and $0.2\,M_\odot$ (dashed). The solid grey line indicates $1\,M_\odot$ enclosed baryonic mass.
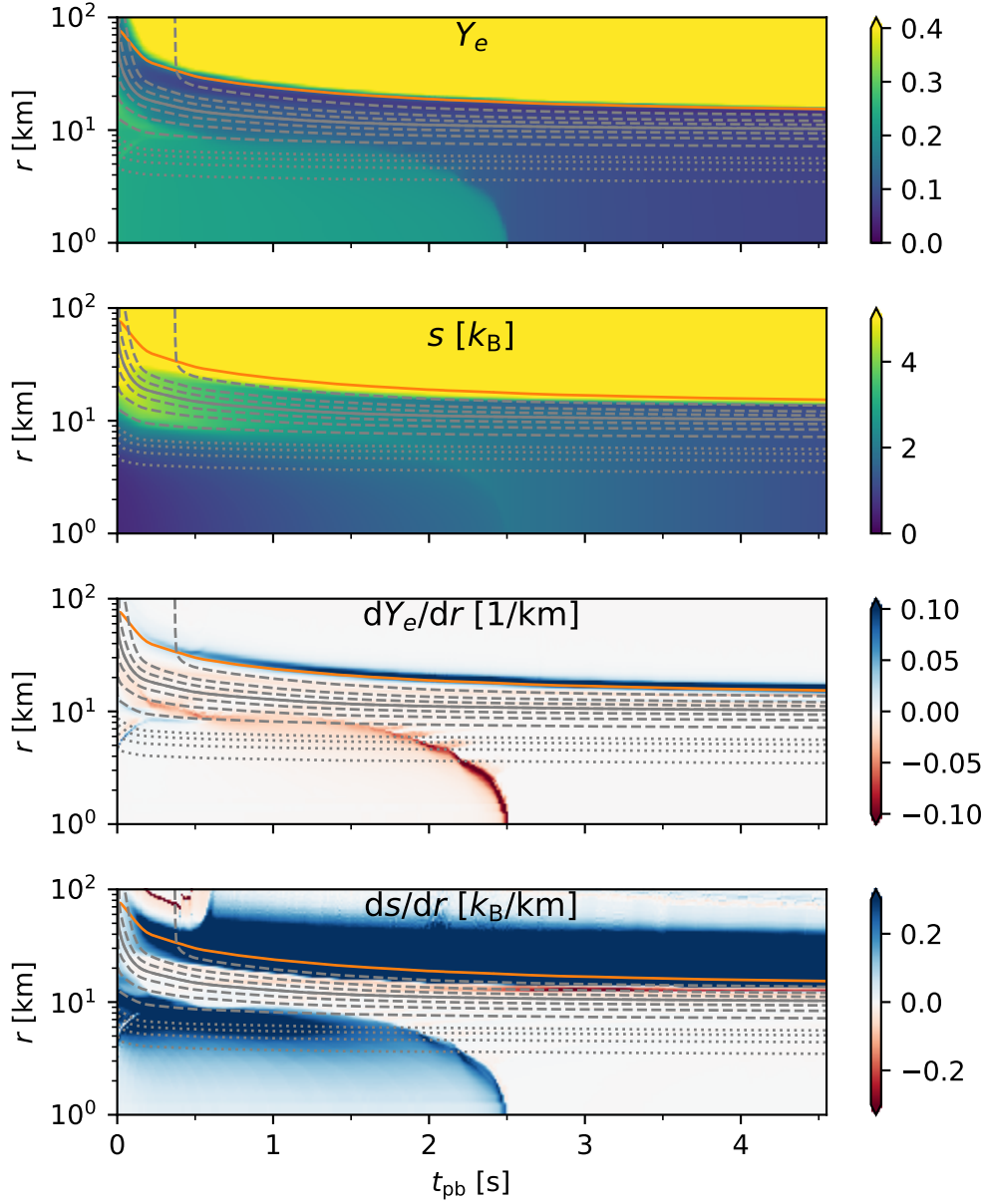
Figure 4.14: Electron fraction and entropy per baryon and radial gradients thereof for model s18.6GR. The orange line indicates the neutron star radius. Grey lines are mass shells of $0.05\,M_\odot$ (dotted) and $0.2\,M_\odot$ (dashed). The solid grey line indicates $1\,M_\odot$ enclosed baryonic mass. As the simulations for this model currently end at $4.55\,\mathrm{s}$ the abscissa has a different scaling compared to the plots of the other models in this section.

Figure 4.15: Electron fraction and entropy per baryon and radial gradients thereof for model s18.6LS. The orange line indicates the neutron star radius. Grey lines are mass shells of $0.05\,\mathrm{M}_\odot$ (dotted) and $0.2\,\mathrm{M}_\odot$ (dashed). The solid grey line indicates $1\,\mathrm{M}_\odot$ enclosed baryonic mass.
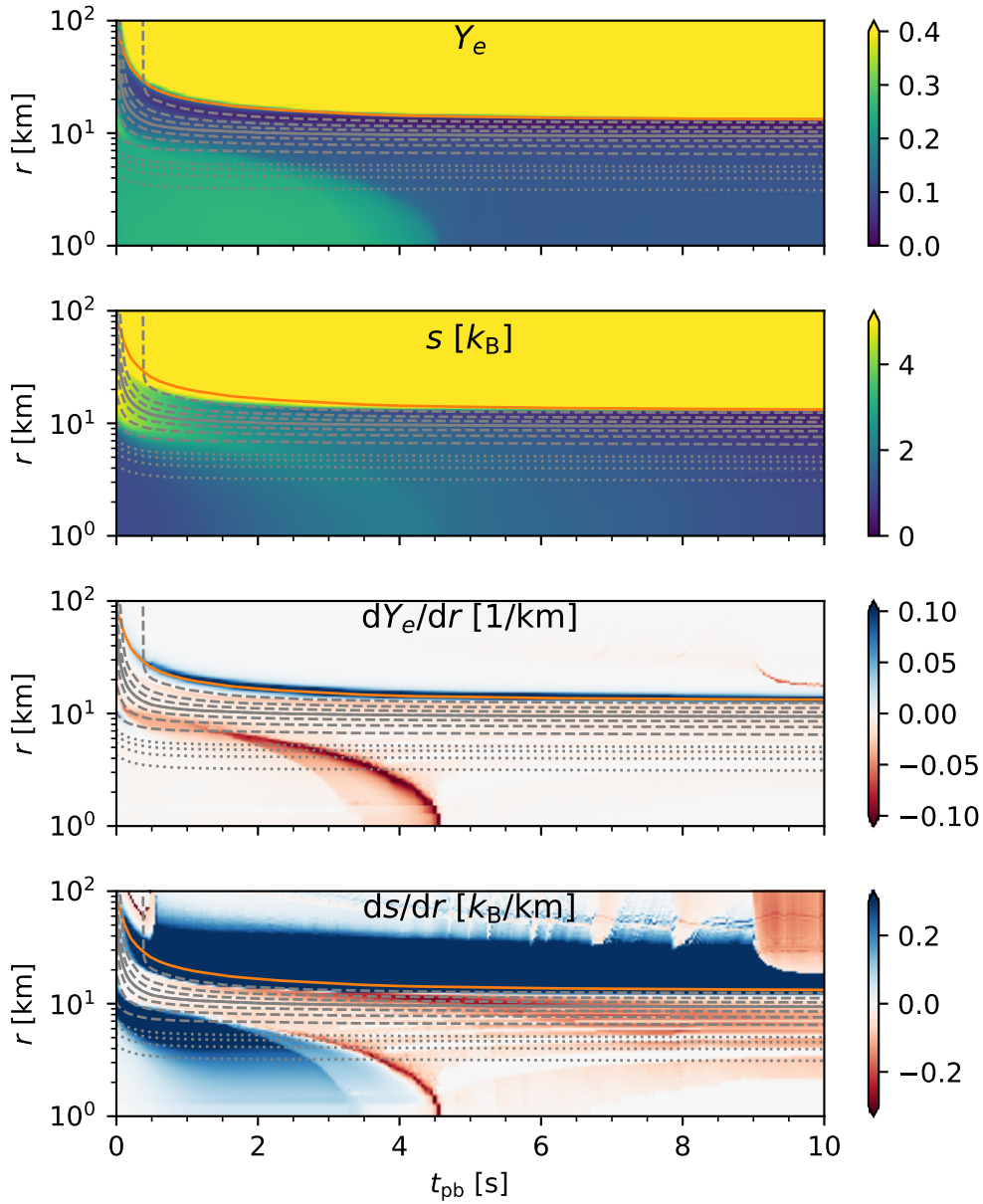
Figure 4.16: Electron fraction and entropy per baryon and radial gradients thereof for model s18.6SO. The orange line indicates the neutron star radius. Grey lines are mass shells of $0.05\,\mathrm{M_\odot}$ (dotted) and $0.2\,\mathrm{M_\odot}$ (dashed). The solid grey line indicates $1\,\mathrm{M_\odot}$ enclosed baryonic mass.
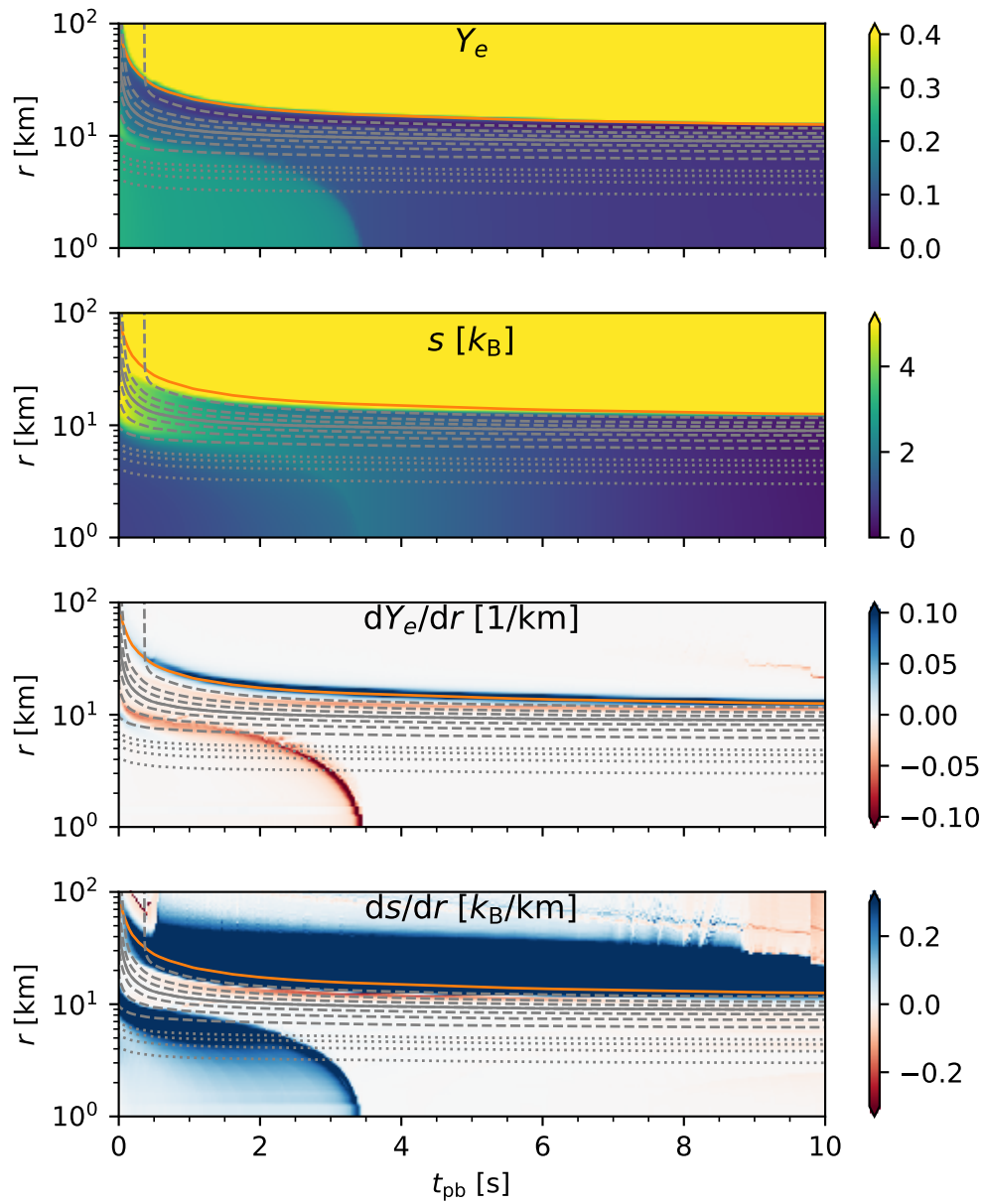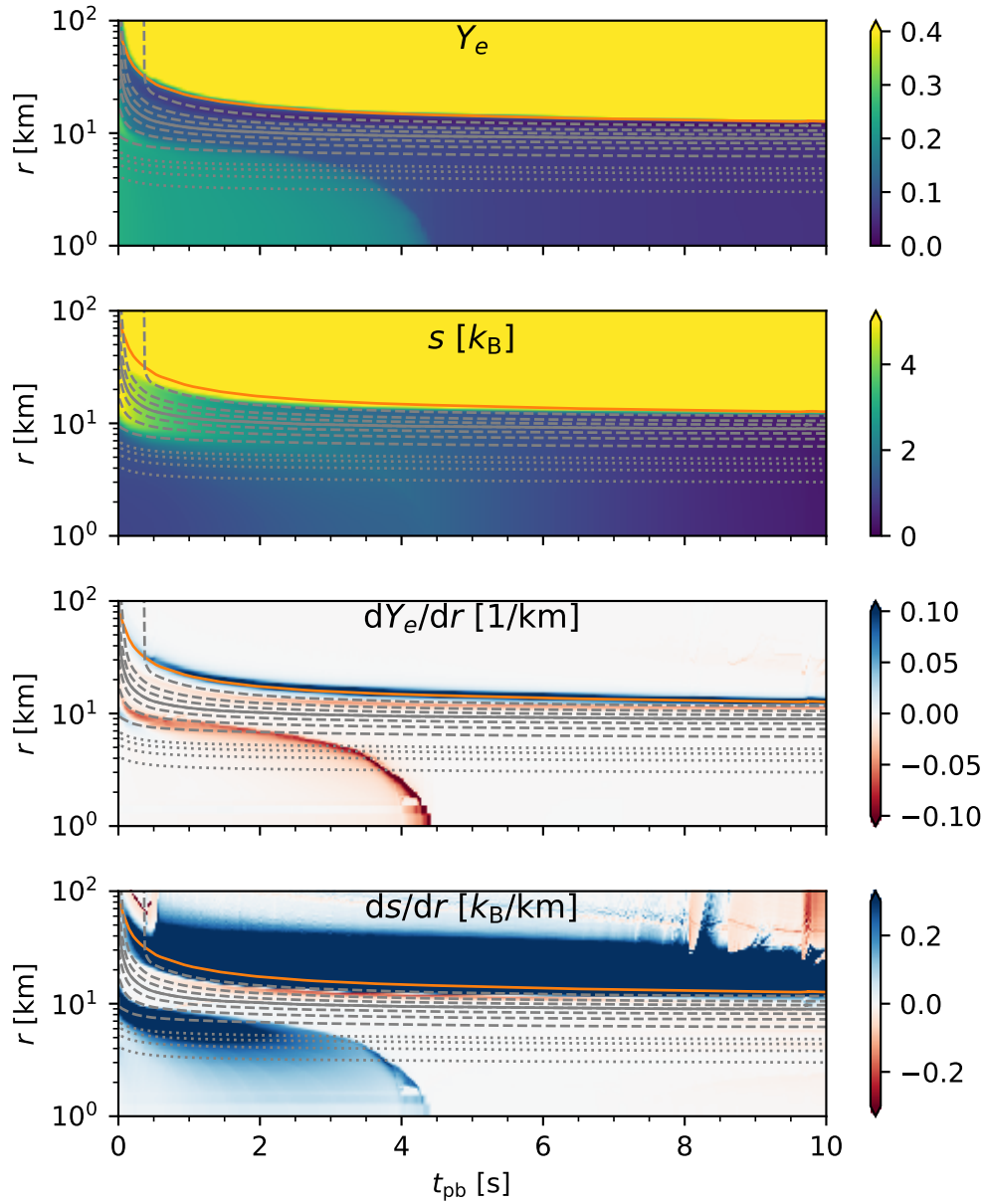
Figure 4.17: Electron fraction and entropy per baryon and radial gradients thereof for model s18.6SX. The orange line indicates the neutron star radius. Grey lines are mass shells of $0.05\,\mathrm{M}_\odot$ (dotted) and $0.2\,\mathrm{M}_\odot$ (dashed). The solid grey line indicates $1\,\mathrm{M}_\odot$ enclosed baryonic mass.
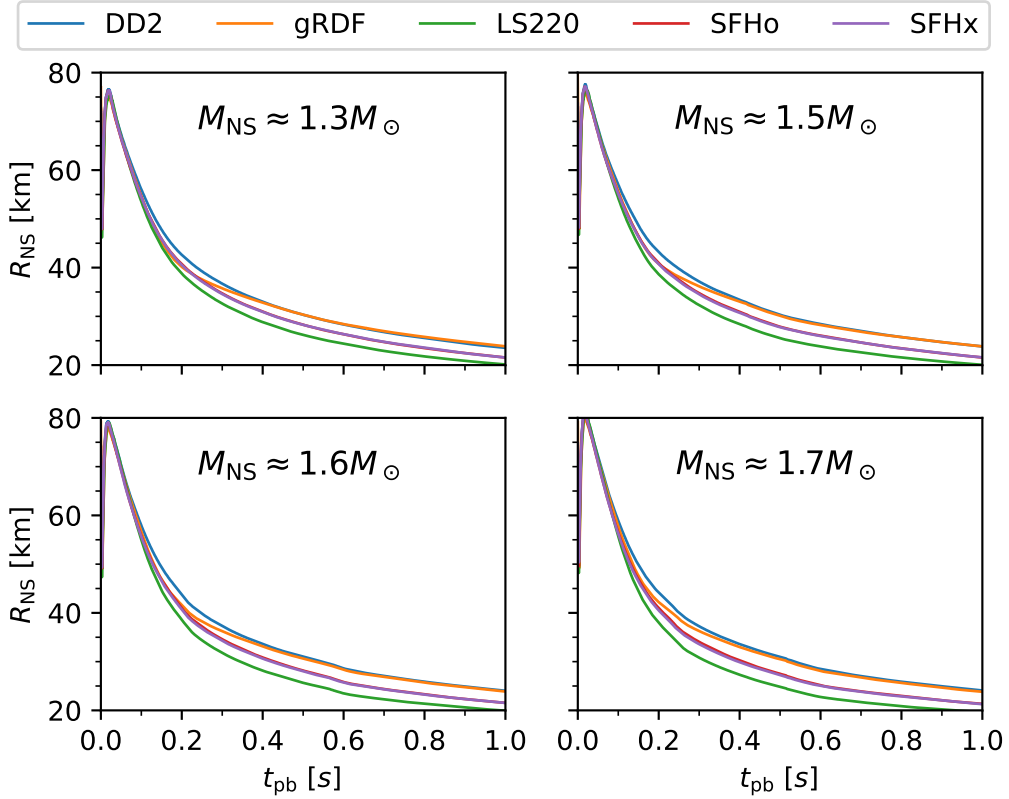
Figure 4.18: Neutron star radius as function of time for different EoS and gravitational neutron star masses. The upper left panel shows models s18.8, the upper right s18.6, the lower left s27.0, and the lower right s20.0.

4.4 Overview over the full Model Set

In this section we give a concise overview over our full model set. Table 4.3 lists the time post bounce each model has reached, the neutron star radius at this time, which we define as the radius where the density has fallen to $10^{11}\,\mathrm{g/cm^3}$, the gravitational neutron star mass at this time, and the total and species specific energies radiated away in neutrinos until the end of our simulations.

In Figures 4.18 and 4.19 we show an overview over the time evolution of the neutron star radius defined as the $10^{11}\,\mathrm{g/cm^3}$ isodensity radius. Over all neutron star masses the EoS dependencies are the same: DD2 and gRDF EoS result in the largest radii at early times. Until approximately 2 s post bounce the DD2 and gRDF yield similar radii, after that the gRDF results in slightly smaller radii. Until 5 s to

Table 4.3: Post bounce time at the current end of the simulation and neutron star radius, neutron star gravitational mass, total and species specific energy emitted by neutrinos at this time. Note that the models with the gRDF EoS are currently calculated until between $3\,\mathrm{s}$ to $5\,\mathrm{s}$, whereas the other models are calculated to $10\,\mathrm{s}$. Therefore the given values for models with the gRDF should not be directly compared with other models. The column M_{NS} shows the values for the 'gravitational' mass as given in the PROMETHEUS-VERTEX output files. However, this is n o t the true gravitaional mass of the neutron star.

| Model | t_{pb} | R_{NS} | M_{NS} | E_{tot} | E_{ν_e} | $E_{\bar{\nu}_e}$ | E_{ν_μ} | $E_{\bar{\nu}_\mu}$ | E_{ν_τ} | $E_{\bar{\nu}_\tau}$ |
	s	km	$M_\odot$	B	B	B	B	B	B	B
s18.8DD	10.0	13.6	1.33	205.0	35.1	32.4	33.6	35.6	33.5	34.8
s18.8GR	4.23	15.2	1.34	184.4	33.8	30.0	30.0	31.6	29.0	30.1
s18.8LS	10.0	13.2	1.33	212.0	35.7	32.5	35.0	37.5	34.9	36.5
s18.8SO	10.0	12.5	1.32	223.6	37.9	34.9	36.8	39.1	36.7	38.2
s18.8SX	10.0	12.5	1.32	224.4	37.9	35.0	37.0	39.3	36.8	38.4
s18.6DD	10.0	13.9	1.48	262.5	46.3	43.5	42.2	44.8	42.0	43.7
s18.6GR	4.55	15.4	1.50	233.3	44.2	40.0	37.0	39.1	35.8	37.2
s18.6LS	10.0	13.3	1.48	267.7	46.8	43.4	43.0	46.4	43.0	45.0
s18.6SO	10.0	12.6	1.47	287.6	50.2	47.1	46.5	49.4	46.2	48.2
s18.6SX	10.0	12.7	1.47	289.5	50.3	47.4	46.9	49.8	46.6	48.6
s27.0DD	10.0	14.0	1.60	314.5	55.6	53.0	50.3	53.5	50.1	52.2
s27.0GR	3.15	16.9	1.64	236.3	46.5	41.6	36.6	39.0	35.5	37.1
s27.0LS	9.29	13.3	1.60	317.4	55.7	52.5	50.7	54.9	50.6	53.0
s27.0SO	10.0	12.7	1.59	345.1	60.4	57.4	55.6	59.1	55.2	57.6
s27.0SX	10.0	12.7	1.59	347.1	60.5	57.6	56.0	59.5	55.5	58.0
s20.0DD	10.0	14.0	1.73	375.2	66.2	63.8	59.9	63.7	59.6	62.1
s20.0GR	4.04	16.3	1.77	304.7	58.7	53.9	47.6	50.6	46.0	48.0
s20.0LS	10.0	13.2	1.73	382.3	67.0	63.8	60.9	66.1	60.7	63.7
s20.0SO	10.1	12.8	1.72	412.3	72.0	69.2	66.3	70.5	65.7	68.6
s20.0SX	10.0	12.9	1.72	415.5	72.2	69.6	66.9	71.2	66.2	69.2
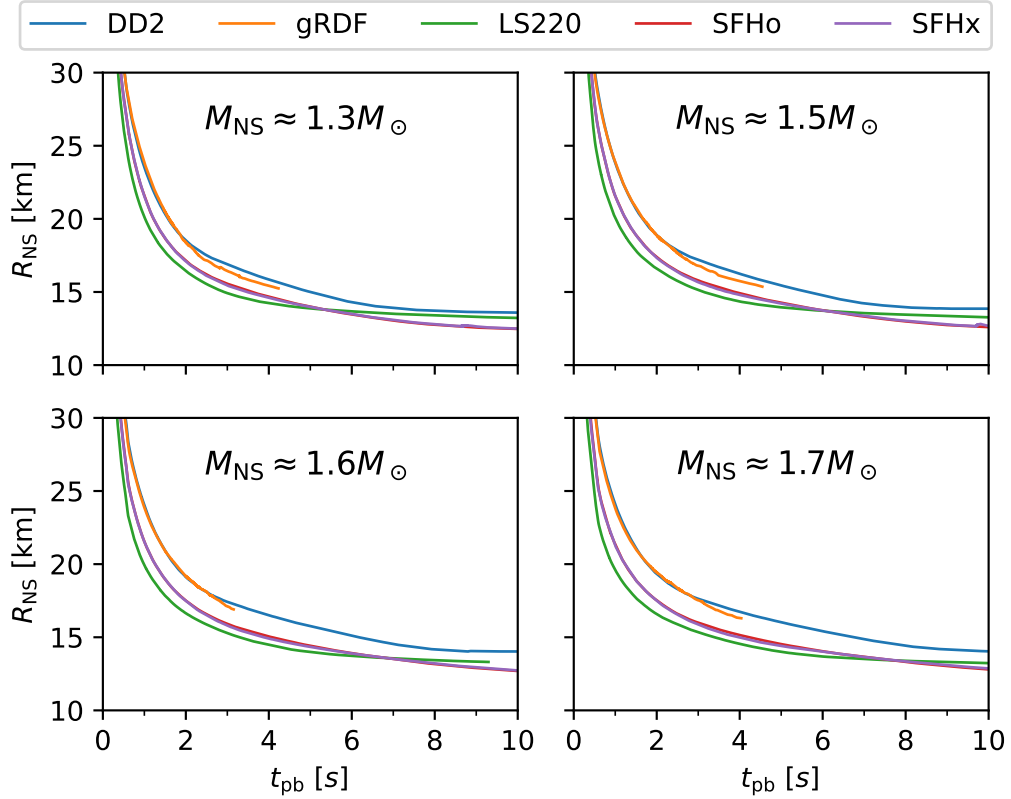
Figure 4.19: Neutron star radius as function of time for different EoS and gravitational neutron star masses. The upper left panel shows models s18.8, the upper right s18.6, the lower left s27.0, and the lower right s20.0.

7 s the LS220 EoS yields the smallest radii, with the very similar results of models with SFHo and SFHx between LS220 and DD2. However at late times a crossing between the models with LS220 and SFHo / SFHx EoS occurs. Hence at the end of our simulations the SFHo and SFHx models yield the smallest radii.

A common way to characterize the neutrino spectra is to use model spectra that reproduce the first two energy moments of the actual spectra. We use the power law spectrum of Keil et al. (2003) given as

$$f_{\alpha,\bar{\epsilon}}(\epsilon) = \frac{(1+\alpha)^{(1+\alpha)}}{\bar{\epsilon} \cdot \Gamma(1+\alpha)} \cdot \left(\frac{\epsilon}{\bar{\epsilon}}\right)^{\alpha} \exp\left\{-(1+\alpha)\frac{\epsilon}{\bar{\epsilon}}\right\} \qquad (4.1)$$

with the parameter alpha determined by

$$\frac{\langle \epsilon^2 \rangle}{\langle \epsilon \rangle^2} = \frac{2 + \alpha}{1 + \alpha} \tag{4.2}$$

and the mean energy $\bar{\epsilon} = \langle \epsilon \rangle$. Here Γ denotes the Euler gamma function. The parameter α can be interpreted as a measure of spectral pinching, i.e. $\alpha = 2$ reproduces a Maxwell-Boltzmann spectrum, $\alpha < 2$ indicates an anti-pinched spectrum with enhanced high energy tail, and $\alpha > 2$ an pinched spectrum with suppressed high energy tail.

The time average of a neutrino radiation quantity $Q(t)$ is computed as

$$\bar{Q} = \frac{\int \mathrm{d}t \, \dot{N}(t) Q(t)}{\int \mathrm{d}t \, \dot{N}(t)} \tag{4.3}$$

where $\dot{N}$ denotes the neutrino number flux, hence we calculate neutrino number weighted time averages. In table 4.4 we list time averaged mean energies and α parameters for our models.

We exclude models with the gRDF EoS from the following discussion, since they are currently only simulated up to $3\,\mathrm{s}$ to $5\,\mathrm{s}$, whereas the other models are simulated to $\approx 10\,\mathrm{s}$. Time integrated quantities of models with gRDF EoS can therefore not be compared with the majority of our model set at the moment.

Figure 4.20 visualizes the dependence of the total energy emitted till the end of our simulations on neutron star mass and EoS. As expected more massive neutron stars release more energy in neutrinos. We can also observe an dependence on the EoS. Since the SFHo and SFHx EoS lead to a smaller neutron star radius compared to the DD2 and LS220 EoS, more gravitational energy is released and emitted in neutrinos.

Figure 4.21 shows the time energies emitted in the different neutrino species till the end of our simulation as function of the neutron star mass for models with different EoS. We can see, that the same dependencies as for the total emitted energy holds, i.e. more neutron star mass and smaller neutron star radius lead to an increase in emitted energy, where the latter depends on the EoS for a given neutron star mass.

Figure 4.22 shows the time averaged mean neutrino energies at the end of our simulations as function of neutron star mass for models with different EoS. The dependency on the neutron star mass is less pronounced as for the emitted energies. The different EoS lead to small differences in the mean energies. Across all neutron star masses and neutrino species the LS220 EoS leads to the highest mean energies, followed by SFHo and SFHx resulting in very similar mean energies, and the DD2 yielding the lowest mean energies. This order differs from the EoS dependence of the energies emitted in neutrinos.
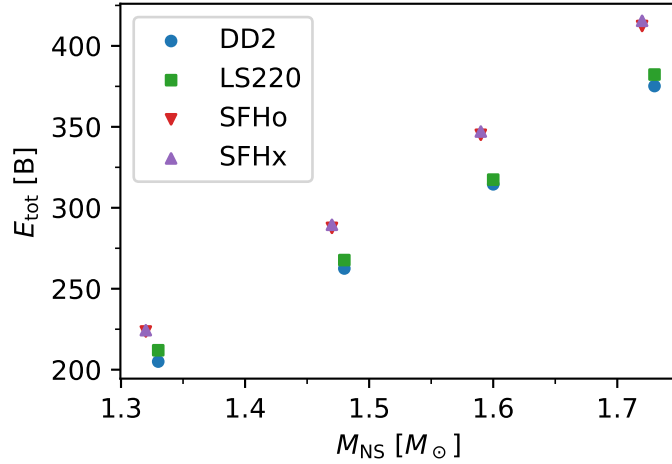
Figure 4.20: Total energy emitted in neutrinos till the end of our simulations ($t_{\mathrm{pb}} \approx$ 10 s) as function of gravitational neutron star mass for the models with DD2, LS220, SFHo, and SFHx EoS. Models with gRDF EoS are not shown since they are currently only simulated up to 3 s to 5 s post bounce and therefore the total emitted energy can not be compared to the other models. The total emitted energy of the SFHo models are very close to the total emitted energies of the SFHx models and therefore overlapping in the plot.

Figure 4.23 shows the time averaged spectral shape parameter alpha as defined by equation (4.2) as function of gravitational neutron star mass for models with different EoS. We see that the spectra of the electron flavoured neutrinos and anti-neutrinos are more pinched than the other flavours. Increasing neutron star mass slightly reduces spectral pinching in all neutrino species. The EoS dependence is weak. Models with the DD2 EoS have slightly more pinched spectra in all neutrino species than models with other EoS.
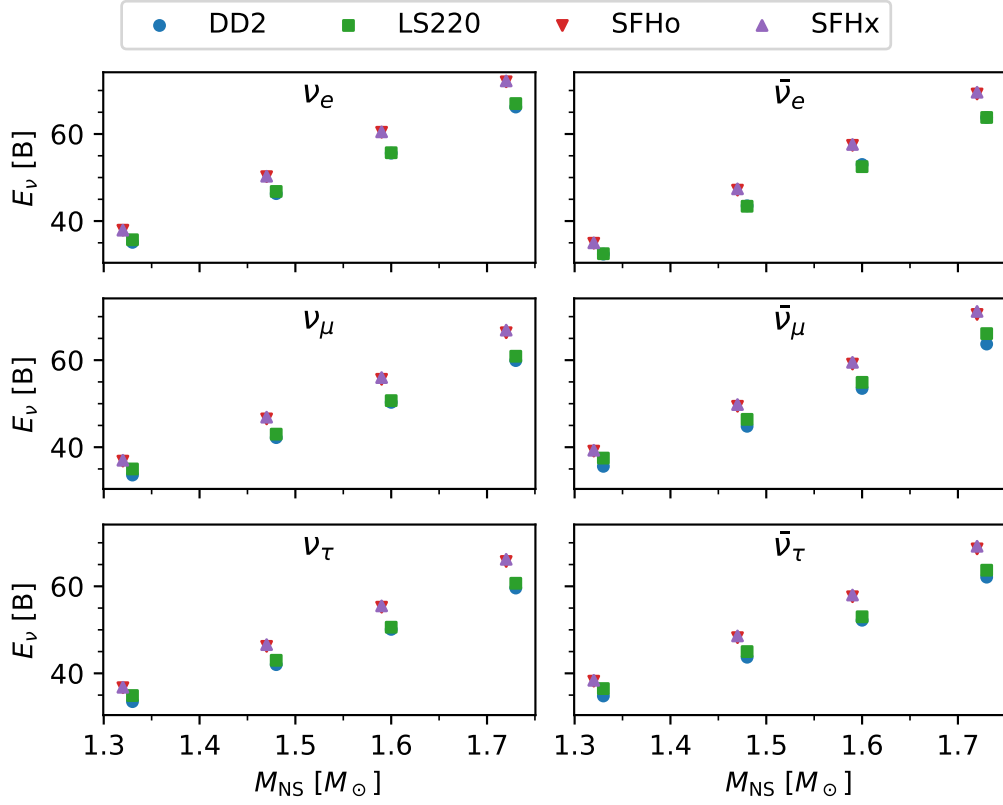
Figure 4.21: Energy emitted in neutrinos of different species till the end of our simulations ($t_{\mathrm{pb}} \approx 10\,\mathrm{s}$) as function of gravitational neutron star mass for the models with DD2, LS220, SFHo, and SFHx EoS. Models with gRDF EoS are not shown since they are currently only simulated until between $3\,\mathrm{s}$ to $5\,\mathrm{s}$ post bounce and therefore the emitted energies cannot be compared to the other models. The emitted energies of the SFHo models are very close to the emitted energies of the SFHx models and therefore overlapping in the plot.
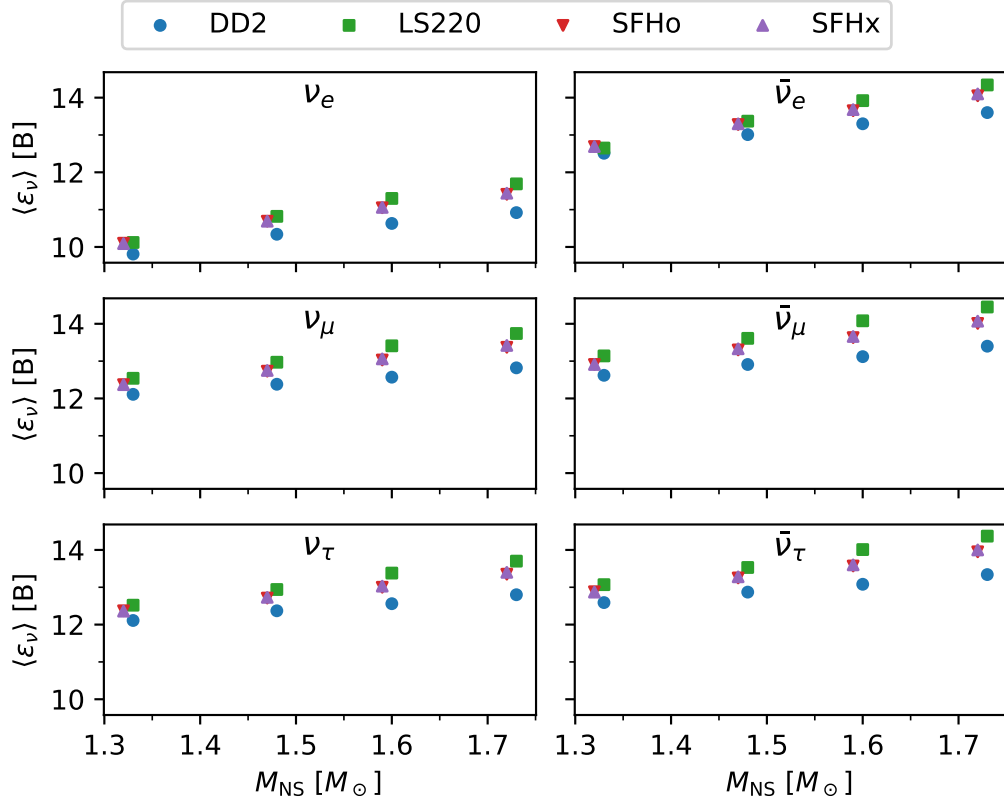
Figure 4.22: Time average of mean neutrino energies at the end of our simulations ($t_{\mathrm{pb}} \approx 10\,\mathrm{s}$) as function of gravitational neutron star mass for the models with DD2, LS220, SFHo, and SFHx EoS. Models with gRDF EoS are not shown since they are currently only simulated until between $3\,\mathrm{s}$ to $5\,\mathrm{s}$ post bounce and therefore the mean energies cannot be compared to the other models. The mean energies of the SFHo models are very close to the mean energies of the SFHx models and therefore overlapping in the plot. The labels are wrong, the mean neutrino energy is shown in MeV!
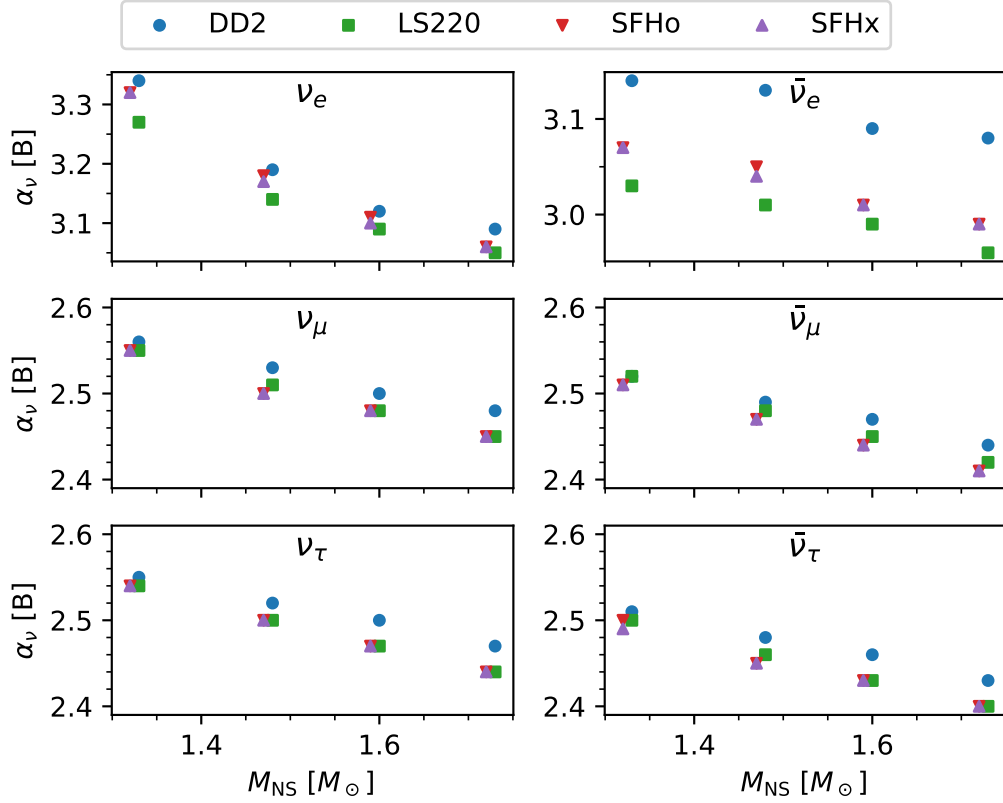
Figure 4.23: Time average of spectral shape parameters as defined by equation 4.2 for the emitted neutrinos at the end of our simulations ($t_{pb} \approx 10\,s$) as function of gravitational neutron star mass for the models with DD2, LS220, SFHo, and SFHx EoS. Models with gRDF EoS are not shown since they are currently only simulated until between $3\,s$ to $5\,s$ post bounce and therefore the spectra cannot be compared to the other models. The alpha parameters of the SFHo models are very close to the alpha parameter of the SFHx models and therefore overlapping in the plot. The labels are wrong, the alpha parameter is unitless. Furthermore this is n o t the spectral shape parameter of the time integrated emission.

Table 4.4: Gravitational neutron star mass, time averaged mean neutrino energies and spectral shape parameters at the end of our simulations. Note that the models with the gRDF EoS are currently calculated until between $3\,\mathrm{s}$ to $5\,\mathrm{s}$, whereas the other models are calculated to $10\,\mathrm{s}$. Therefore the given values for models with the gRDF should not be directly compared with other models. The spectral shape parameter is n o t the spectral shape of the time integrated emission.

| Model | M_{NS} | $\langle\epsilon_{\nu_e}\rangle$ | $\langle\epsilon_{\bar{\nu}_e}\rangle$ | $\langle\epsilon_{\nu_\mu}\rangle$ | $\langle\epsilon_{\bar{\nu}_\mu}\rangle$ | $\langle\epsilon_{\nu_\tau}\rangle$ | $\langle\epsilon_{\bar{\nu}_\tau}\rangle$ | α_{ν_e} | $\alpha_{\bar{\nu}_e}$ | α_{ν_μ} | $\alpha_{\bar{\nu}_\mu}$ | α_{ν_τ} | $\alpha_{\bar{\nu}_\tau}$ |
	$\mathrm{M}_\odot$	MeV	MeV	MeV	MeV	MeV	MeV	1	1	1	1	1	1
s18.8DD	1.33	9.81	12.51	12.11	12.62	12.11	12.59	3.34	3.14	2.56	2.52	2.55	2.51
s18.8GR	1.34	10.34	12.95	12.87	13.31	12.78	13.26	3.45	3.19	2.57	2.49	2.53	2.47
s18.8LS	1.33	10.12	12.65	12.54	13.14	12.52	13.07	3.27	3.03	2.55	2.52	2.54	2.50
s18.8SO	1.32	10.10	12.69	12.37	12.91	12.37	12.88	3.32	3.07	2.55	2.51	2.54	2.50
s18.8SX	1.32	10.09	12.69	12.37	12.91	12.36	12.87	3.32	3.07	2.55	2.51	2.54	2.49
s18.6DD	1.48	10.34	13.01	12.38	12.91	12.37	12.87	3.19	3.13	2.53	2.49	2.52	2.48
s18.6GR	1.50	10.91	13.51	13.19	13.66	13.10	13.61	3.29	3.17	2.54	2.45	2.49	2.43
s18.6LS	1.48	10.82	13.37	12.97	13.61	12.94	13.53	3.14	3.01	2.51	2.48	2.50	2.46
s18.6SO	1.47	10.69	13.28	12.73	13.30	12.71	13.25	3.18	3.05	2.50	2.47	2.50	2.45
s18.6SX	1.47	10.69	13.30	12.75	13.33	12.73	13.28	3.17	3.04	2.50	2.47	2.50	2.45
s27.0DD	1.60	10.63	13.30	12.57	13.12	12.56	13.08	3.12	3.09	2.50	2.47	2.50	2.46
s27.0GR	1.64	11.36	14.13	13.72	14.29	13.66	14.23	3.26	3.27	2.55	2.48	2.51	2.46
s27.0LS	1.60	11.30	13.92	13.41	14.08	13.38	14.01	3.09	2.99	2.48	2.45	2.47	2.43
s27.0SO	1.59	11.05	13.65	13.03	13.63	13.00	13.57	3.11	3.01	2.48	2.44	2.47	2.43
s27.0SX	1.59	11.06	13.68	13.06	13.66	13.03	13.60	3.10	3.01	2.48	2.44	2.47	2.43
s20.0DD	1.73	10.92	13.60	12.82	13.40	12.80	13.34	3.09	3.08	2.48	2.44	2.47	2.43
s20.0GR	1.77	11.63	14.35	13.88	14.44	13.80	14.38	3.20	3.19	2.51	2.44	2.47	2.42
s20.0LS	1.73	11.69	14.34	13.74	14.45	13.70	14.37	3.05	2.96	2.45	2.42	2.44	2.40
s20.0SO	1.72	11.41	14.05	13.37	14.01	13.35	13.95	3.06	2.99	2.45	2.41	2.44	2.40
s20.0SX	1.72	11.44	14.10	13.42	14.07	13.40	14.00	3.06	2.99	2.45	2.41	2.44	2.40

Chapter 5

Conclusions and Outlook

In this master thesis project we conducted and analysed a set of neutrino-cooling simulations for proto-neutron stars (PNS) of different masses, using a variety of modern hadronic nuclear equations of state (EoS) models to describe the physical conditions, i.e. thermodynamic state and particle composition, in the hot supra-nuclear medium. We also included muons in the plasma and for neutrino interactions. All of our considered finite-temperature EoS are compatible with experimental and astrophysical constraints, including the best measured lower limits for the maximum neutron star mass, the most recent radius limits deduced from gravitational-wave measurements of neutron star merger events and X-ray measurements by the Neutron Star Interior Composition Explorer (NICER) on the International Space Station. Despite this compatibility, the considered EoS models lead to considerably different mass-radius relations for cold neutron stars and predict maximum gravitational neutron star masses between about $2.05\,\mathrm{M}_\odot$ and $2.4\,\mathrm{M}_\odot$.

The simulations of stellar core collapse, PNS formation, and subsequent PNS cooling were performed with the neutrino-hydrodynamics code PROMETHEUS-VERTEX (Rampp and Janka 2002) in its most recent version (Bollig et al. 2017, Bollig 2018), assuming spherical symmetry, but including a treatment of convection by using the mixing-length approximation. Since supernova explosions by the neutrino-driven mechanism require the presence of multi-dimensional hydrodynamic instabilities (convective overturn, turbulent flows, and the standing accretion shock instability) the explosion was triggered artificially in our spherically symmetric models such that neutron stars with chosen baryonic masses were obtained. Our goal of constructing an initial library of 20 models with 4 different neutron star masses and 5 different EoS, whose evolution needs to be computed for at least 10 seconds, would not be feasible in three dimensions with currently available supercomputing resources. Moreover, the library of models is planned to be extended continuously over the coming years.

The main goals of this project are improved predictions of the neutrino signal that can be measured from a future supernova in the Milky Way. Furthermore the predictions can be employed for theoretical modelling of the diffuse supernova neutrino background (DSNB).

As a next step it is planned to use the results of this study for a comparison with the so far only detection of supernova neutrinos from SN1987A. Our models, computed with state-of-the-art descriptions of the nuclear EoS, Boltzmann neutrino transport, a most refined treatment of neutrino interactions taking muons into account, and PNS convection will permit a revision of the conclusions drawn from the SN1987A neutrino data, including a revised view on the puzzles connected to some signal features, for example the 7 seconds gap in the Kamiokande II data and the marginal compatibility between the events reported by the Kamiokande II and Irvine-Michigan-Brookhaven (IMB) experiments. In this context it is most interesting that in our calculations electron anti-neutrinos as well as muon and tau neutrinos are considerably less energetic than predicted by the astrophysical models used for the first interpretations of the SN1987A neutrino data. The reason for this finding is the inclusion or improvement of a larger set of neutrino reactions that were either ignored or treated only approximately in earlier models, for example neutrino-nucleon scatterings were only considered as iso-energetic reactions.

In another line of follow-up work, our repository of neutrino signals from stellar core collapse will be expanded by adding a bigger grid of neutron star masses and also including black hole formation cases. A large library of such self-consistently computed neutrino signals will help to consolidate the predictions of the DSNB with respect to the necessary input of source signals from supernova models. Our results contain already a number of interesting messages. While we find the expected increase of the energy release in neutrinos with increasing neutron star mass and a subdominant variation with the nuclear EoS (softer EoS leading to a smaller final neutron star radius and hence more energy release), we witness only a rather weak dependence of the neutrino spectra on the neutron star mass and EoS, and an even weaker variation of the spectral shape parameter α, which measures the width of the time-integrated source spectrum or, in other words, its deviation from a Maxwell-Boltzmann spectrum. Our results strengthen assumptions that had to be made because of a lack of systematic, detailed calculations for the neutrino source spectra adopted in a recent comprehensive theoretical investigation of the DSNB by Kresse et al. (2021).

Bibliography

Abbott, B. P. et al. (2017). »GW170817: Observation of Gravitational Waves from a Binary Neutron Star Inspiral«. In: *Physical Review Letters* 119.16. DOI: `10.1103/PhysRevLett.119.161101`.

Abbott, B. P. et al. (2018). »GW170817: Measurements of Neutron Star Radii and Equation of State«. In: *Physical Review Letters* 121 (16). DOI: `10.1103/PhysRevLett.121.161101`.

Alexeyev, E. N. et al. (1988). »Detection of the neutrino signal from SN 1987A in the LMC using the INR Baksan underground scintillation telescope«. In: *Physics Letters B* 205.2-3. DOI: `10.1016/0370-2693(88)91651-6`.

Antoniadis, John et al. (2013). »A Massive Pulsar in a Compact Relativistic Binary«. In: *Science* 340.6131. DOI: `10.1126/science.1233232`.

Bauswein, A. et al. (2017). »Neutron-star Radius Constraints from GW170817 and Future Detections«. In: *Astrophysical Journal Letters* 850.2. DOI: `10.3847/2041-8213/aa9994`.

Bionta, R. M. et al. (1987). »Observation of a neutrino burst in coincidence with supernova 1987A in the Large Magellanic Cloud«. In: *Physical Review Letters* 58.14. DOI: `10.1103/PhysRevLett.58.1494`.

Bollig, R. (2018). »Muon Creation and Effects in Supernovae«. PhD thesis. Technische Universität München.

Bollig, R. et al. (2017). »Muon Creation in Supernova Matter Facilitates Neutrino-Driven Explosions«. In: *Physical Review Letters* 119.24. DOI: `10.1103/PhysRevLett.119.242702`.

Bollig, R. et al. (2021). »Self-consistent 3D Supernova Models From -7 Minutes to +7 s: A 1-bethe Explosion of a 19 $M_\odot$ Progenitor«. In: *Astrophysical Journal* 915.1. DOI: `10.3847/1538-4357/abf82e`.

Bruenn, S. W. (1985). »Stellar core collapse - Numerical model and infall epoch«. In: *Astrophysical Journal Supplement Series* 58. DOI: `10.1086/191056`.

Bruenn, S. W. and Mezzacappa, A. (1997). »Ion screening effects and stellar collapse«. In: *Physical Review D* 56.12. DOI: `10.1103/PhysRevD.56.7529`.

Buras, R. et al. (2003). »Electron Neutrino Pair Annihilation: A New Source for Muon and Tau Neutrinos in Supernovae«. In: *The Astrophysical Journal* 587.1. DOI: `10.1086/368015`.

Buras, R. et al. (2006). »Two-dimensional hydrodynamic core-collapse supernova simulations with spectral neutrino transport. I. Numerical method and results for

a 15 M⊙ star«. In: *Astronomy and Astrophysics* 447.3. DOI: `10.1051/0004-6361: 20053783`.

Burrows, A. (1984). »On detecting stellar collapse with neutrinos«. In: *Astrophysical Journal* 283. DOI: `10.1086/162371`.

– (1987). »Convection and the Mechanism of Type II Supernovae«. In: *Astrophysical Journal Letter* 318. DOI: `10.1086/184937`.

– (1990). »Neutrinos from Supernovae«. In: *Supernovae.* Springer New York. DOI: `10.1007/978-1-4612-3286-5_7`.

Burrows, A. and Lattimer, J. M. (1986). »The Birth of Neutron Stars«. In: *Astrophysical Journal* 307. DOI: `10.1086/164405`.

Burrows, A. and Sawyer, R. F. (1998). »Effects of correlations on neutrino opacities in nuclear matter«. In: *Physical Review C* 58.1. DOI: `10.1103/PhysRevC.58.554`.

– (1999). »Many-body corrections to charged-current neutrino absorption rates in nuclear matter«. In: *Physical Review C* 59.1. DOI: `10.1103/PhysRevC.59.510`.

Carter, G. W. and Prakash, M. (2002). »The quenching of the axial coupling in nuclear and neutron-star matter«. In: *Physics Letters B* 525.3-4. DOI: `10.1016/S0370-2693(01)01452-6`.

Chernohorsky, J. (1994). »Symmetries in Neutrino-Electron Scattering«. In: *Astrophysical Journal* 433. DOI: `10.1086/174639`.

Colella, P. and Woodward, P.R. (1984). »The Piecewise Parabolic Method (PPM) for Gas-Dynamical Simulations«. In: *Journal of Computational Physics* 54.

Cromartie, H. T. et al. (2020). »Relativistic Shapiro delay measurements of an extremely massive millisecond pulsar«. In: *Nature Astronomy* 4. DOI: `10.1038/s41550-019-0880-2`.

Epstein, R. I. (1979). »Lepton-driven convection in supernovae.« In: *Monthly Notices of the Royal Astronomical Society* 188. DOI: `10.1093/mnras/188.2.305`.

Fiorella, B. G. and Fantina, A. F. (2018). »Nuclear Equation of State for Compact Stars and Supernovae«. In: *The Physics and Astrophysics of Neutron Stars.* Springer International Publishing. DOI: `10.1007/978-3-319-97616-7_6`.

Fischer, T. et al. (2014). »Symmetry energy impact in simulations of core-collapse supernovae«. In: *European Physical Journal A* 50. DOI: `10.1140/epja/i2014-14046-5`.

Fryxell, B. A., Müller, E. and Arnett, D. (1989). »Hydrodynamics and Nuclear Burning«.

Hannestad, S. and Raffelt, G. (1998). »Supernova Neutrino Opacity from Nucleon-Nucleon Bremsstrahlung and Related Processes«. In: *The Astrophysical Journal* 507.1. DOI: `10.1086/306303`.

Hempel, M. and Schaffner-Bielich, J. (2010). »A statistical model for a complete supernova equation of state«. In: *Nuclear Physics A* 837.3-4. DOI: `10.1016/j.nuclphysa.2010.02.010`.

Hirata, K. et al. (1987). »Observation of a neutrino burst from the supernova SN1987A«. In: *Physical Review Letters* 58.14. DOI: `10.1103/PhysRevLett.58.1490`.

Horowitz, C. J. (1997). »Neutrino trapping in a supernova and the screening of weak neutral currents«. In: *Physical Review D* 55.8. DOI: `10.1103/PhysRevD.55.4577`.

– (2002). »Weak magnetism for antineutrinos in supernovae«. In: *Physical Review D* 65 (4). DOI: `10.1103/PhysRevD.65.043001`.

Horowitz, C. J. et al. (2017). »Neutrino-nucleon scattering in supernova matter from the virial expansion«. In: *Physical Review C* 95.2. DOI: `10.1103/PhysRevC.95.025801`.

Hüdepohl, L. (2013). »Neutrinos from the Formation, Cooling and Black Hole Collapse of Neutron Stars«. PhD thesis. Technische Universität München.

Hüdepohl, L. et al. (2010). »Neutrino Signal of Electron-Capture Supernovae from Core Collapse to Cooling«. In: *Physical Review Letter* 104.25. DOI: `10.1103/PhysRevLett.104.251101`.

Janka, H.-T. (1995).

Janka, H.-T., Kifonidis, K. and Rampp, M. (2001). »Supernova Explosions and Neutron Star Formation«. In: *Physics of Neutron Star Interiors*. Ed. by D. Blaschke, N. K. Glendenning and A. Sedrakian. Vol. 578.

Keil, M. T., Raffelt, G. G. and Janka, H.-T. (2003). »Monte Carlo Study of Supernova Neutrino Spectra Formation«. In: *Astrophysical Journal* 590.2. DOI: `10.1086/375130`.

Keil, W. (1997). »Konvektive Instabilitäten in entstehenden Neutronensternen«. PhD thesis. Technische Universität München.

Keil, W. and Janka, H.-T. (1995). »Hadronic phase transitions at supranuclear densities and the delayed collapse of newly formed neutron stars.« In: *Astronomy and Astrophysics* 296.

Keil, W., Janka, H.-T. and Müller, E. (1996). »Ledoux Convection in Protoneutron Stars—A Clue to Supernova Nucleosynthesis?« In: *Astrophysical Journal Letters* 473. DOI: `10.1086/310404`.

Kifonidis, K. et al. (2003). »Non-spherical core collapse supernovae. I. Neutrino-driven convection, Rayleigh-Taylor instabilities, and the formation and propagation of metal clumps«. In: *Astronomy and Astrophysics* 408, pp. 621–649.

Kresse, D., Ertl, T. and Janka, H.-T. (2021). »Stellar Collapse Diversity and the Diffuse Supernova Neutrino Background«. In: *Astrophysical Journal* 909.2. DOI: `10.3847/1538-4357/abd54e`.

Langanke, K. et al. (2003). »Electron Capture Rates on Nuclei and Implications for Stellar Core Collapse«. In: *Physical Review Letters* 90.24. DOI: `10.1103/PhysRevLett.90.241102`.

Langanke, K. et al. (2008). »Effects of Inelastic Neutrino-Nucleus Scattering on Supernova Dynamics and Radiated Neutrino Spectra«. In: *Physical Review Letters* 100.1. DOI: `10.1103/PhysRevLett.100.011101`.

Lattimer, J. M. and Swesty, D. F. (1991). »A generalized equation of state for hot, dense matter«. In: *Nuclear Physics A* 535.2.

Liebendörfer, M. et al. (2005). »Supernova Simulations with Boltzmann Neutrino Transport: A Comparison of Methods«. In: *Astrophysical Journal* 620.2. DOI: `10.1086/427203`.

Lohs, A. (2015). »Neutrino Reactions in Hot and Dense Matter«. PhD thesis. TU Darmstadt.

Marek, A. et al. (2006). »Exploring the relativistic regime with Newtonian hydrodynamics: an improved effective gravitational potential for supernova simulations«. In: *Astronomy and Astrophysics* 445.1.

Martinez-Pinedo, G. et al. (2012). »Charged-Current Weak Interaction Processes in Hot and Dense Matter and its Impact on the Spectra of Neutrinos Emitted from Protoneutron Star Cooling«. In: *Physical Review Letters* 109.25. DOI: `10.1103/PhysRevLett.109.251104`.

Mezzacappa, A. and Bruenn, S. W. (1993). »Stellar Core Collapse: A Boltzmann Treatment of Neutrino-Electron Scattering«. In: *Astrophysical Journal* 410. DOI: `10.1086/172791`.

Miller, M. C. et al. (2019). »PSR J0030+0451 Mass and Radius from NICER Data and Implications for the Properties of Neutron Star Matter«. In: *Astrophysical Journal Letters* 887.1. DOI: `10.3847/2041-8213/ab50c5`.

Mirizzi, A. et al. (2016). »Supernova neutrinos: production, oscillations and detection«. In: *Nuovo Cimento Rivista Serie* 39.1-2. DOI: `10.1393/ncr/i2016-10120-8`.

Müller, B., Janka, H.-T. and Dimmelmeier, H. (2010). »A New Multi-dimensional General Relativistic Neutrino Hydrodynamic Code for Core-collapse Supernovae. I. Method and Code Tests in Spherical Symmetry«. In: *Astrophysical Journal Supplement* 189.1. DOI: `10.1088/0067-0049/189/1/104`.

Nagakura, H., Burrows, A. and Vartanyan, D. (2021). »Supernova neutrino signals based on long-term axisymmetric simulations«. In: *Monthly Notices of the Royal Astronomical Society* 506.1. DOI: `10.1093/mnras/stab1785`.

Nakazato, K. et al. (2022). »Observing Supernova Neutrino Light Curves with Super-Kamiokande. II. Impact of the Nuclear Equation of State«. In: *Astrophysical Journal* 925.1. DOI: `10.3847/1538-4357/ac3ae2`.

O'Connor, E. et al. (2018). »Global comparison of core-collapse supernova simulations in spherical symmetry«. In: *Journal of Physics G* 45.10. DOI: `10.1088/1361-6471/aadeae`.

Oertel, M. et al. (2017). »Equations of state for supernovae and compact stars«. In: *Reviews of Modern Physics* 89.1.

Pais, H. and Typel, S. (2017). »Comparsion of Equation of State Models with Different Cluster Dissolution Mechanisms«. In: *Nuclear Particle Correlations and Cluster Physics*. Chap. Chapter 4, pp. 95–132. DOI: `10.1142/9789813209350_0004`.

Plewa, T. and Müller, E. (1999). »The consistent multi-fluid advection method«. In: *Astronomy and Astrophysics* 342.

Pons, J. A., Miralles, J. A. and Ibanez, J. M. A. (1998). »Legendre expansion of the neutrino anti-neutrino - electron positron kernel«. In: *Astronomy and Astrophysics Supplement* 129. DOI: `10.1051/aas:1998189`.

Pons, J. A. et al. (1999). »Evolution of Proto-Neutron Stars«. In: *Astrophysical Journal* 513.2. DOI: `10.1086/306889`.

Pons, J. A. et al. (2001a). »Evolution of Proto-Neutron Stars with Kaon Condensates«. In: *Astrophysical Journal* 553.1. DOI: `10.1086/320642`.

Pons, J. A. et al. (2001b). »Evolution of Proto-Neutron Stars with Quarks«. In: *Physical Review Letters* 86.23. DOI: `10.1103/PhysRevLett.86.5223`.

Rampp, M. (2000). »Radiation Hydrodynamics with Neutrinos: Stellar Core Collapse and the Explosion Mechanism of Type II Supernovae«. PhD thesis. Technische Universität München.

Rampp, M. and Janka, H.-T. (2002). »Radiation hydrodynamics with neutrinos. Variable Eddington factor method for core-collapse supernova simulations«. In: *Astronomy and Astrophysics* 396.

Reddy, S. et al. (1999). »Effects of strong and electromagnetic correlations on neutrino interactions in dense matter«. In: *Physical Review C* 59.5. DOI: `10.1103/PhysRevC.59.2888`.

Riley, T. E. et al. (2019). »A NICER View of PSR J0030+0451: Millisecond Pulsar Parameter Estimation«. In: *Astrophysical Journal Letters* 887.1. DOI: `10.3847/2041-8213/ab481c`.

Roberts, L. F. and Reddy, S. (2016). »Neutrino Signatures from Young Neutron Stars«. In: *Handbook of Supernovae*. Springer International Publishing. DOI: `10.1007/978-3-319-20794-0_5-1`.

Roberts, L. F., Reddy, Sanjay and Shen, Gang (2012a). »Medium modification of the charged-current neutrino opacity and its implications«. In: *Physical Review C* 86.6. DOI: `10.1103/PhysRevC.86.065803`.

Roberts, L. F. et al. (2012b). »Protoneutron Star Cooling with Convection: The Effect of the Symmetry Energy«. In: *Physical Review Letters* 108.6. DOI: `10.1103/PhysRevLett.108.061103`.

Romani, R. W. et al. (2021). »PSR J1810+1744: Companion Darkening and a Precise High Neutron Star Mass«. In: *The Astrophysical Journal Letters* 908.2, L46. DOI: `10.3847/2041-8213/abe2b4`.

Shlomo, S., Kolomietz, V. M. and Colò, G. (2006). »Deducing the nuclear-matter incompressibility coefficient from data on isoscalar compression modes«. In: *The European Physical Journal A* 30. DOI: 10.1140/epja/i2006-10100-3.

Steiner, A. W., Hempel, M. and Fischer, T. (2013). »Core-collapse Supernova Equations of State Based on Neutron Star Observations«. In: *The Astrophysical Journal* 774.1. DOI: 10.1088/0004-637X/774/1/17.

Steiner, A. W., Lattimer, J. M. and Brown, E. F. (2010). »The Equation of State from Observed Masses and Radii of Neutron Stars«. In: *The Astrophysical Journal* 722.1. DOI: 10.1088/0004-637X/722/1/33.

Stone, J. R., Stone, N. J. and Moszkowski, S. A. (2014). »Incompressibility in finite nuclei and nuclear matter«. In: *Physical Review C* 89.4. DOI: 10.1103/PhysRevC.89.044316.

Sukhbold, T., Woosley, S. E. and Heger, A. (2018). »A High-resolution Study of Presupernova Core Structure«. In: *The Astrophysical Journal* 860.2. DOI: 10.3847/1538-4357/aac2da.

Sumiyoshi, K., Suzuki, H. and Toki, H. (1995). »Influence of the symmetry energy on the birth of neutron stars and supernova neutrinos.« In: *Astronomy and Astrophysics* 303.

Suzuki, H. (1993). »Supernova neutrinos - multigroup simulations of neutrinos from protoneutron star.« In: *Frontiers of Neutrino Astrophysics.*

Suzuki, H. and Sato, K. (1991). »Multigroup Simulation of Protoneutron Star Cooling«. In: *Supernovae.* Ed. by Stanford E. Woosley, p. 324.

Typel, S. (2018). »Equations of state for astrophysical simulations from generalized relativistic density functionals«. In: *Journal of Physics G: Nuclear and Particle Physics* 45.11.

Typel, S. et al. (2010). »Composition and thermodynamics of nuclear matter with light clusters«. In: *Physical Review C* 81.1. DOI: 10.1103/PhysRevC.81.015803.

Wilson, J. R. and Mayle, R. W. (1988). »Convection in core collapse supernovae.« In: *Physics Reports* 163.1. DOI: 10.1016/0370-1573(88)90036-1.

Woosley, S. E. and Heger, A. (2007). »Nucleosynthesis and remnants in massive stars of solar metallicity«. In: *Physics Reports* 442.1-6. DOI: 10.1016/j.physrep.2007.02.009.

Woosley, S. E., Heger, A. and Weaver, T. A. (2002). »The evolution and explosion of massive stars«. In: *Reviews of Modern Physics* 74 (4). DOI: 10.1103/RevModPhys.74.1015.

Yamada, S., Janka, H.-T. and Suzuki, H. (1999). »Neutrino transport in type II supernovae: Boltzmann solver vs. Monte Carlo method«. In: *Astronomy and Astrophysics* 344.